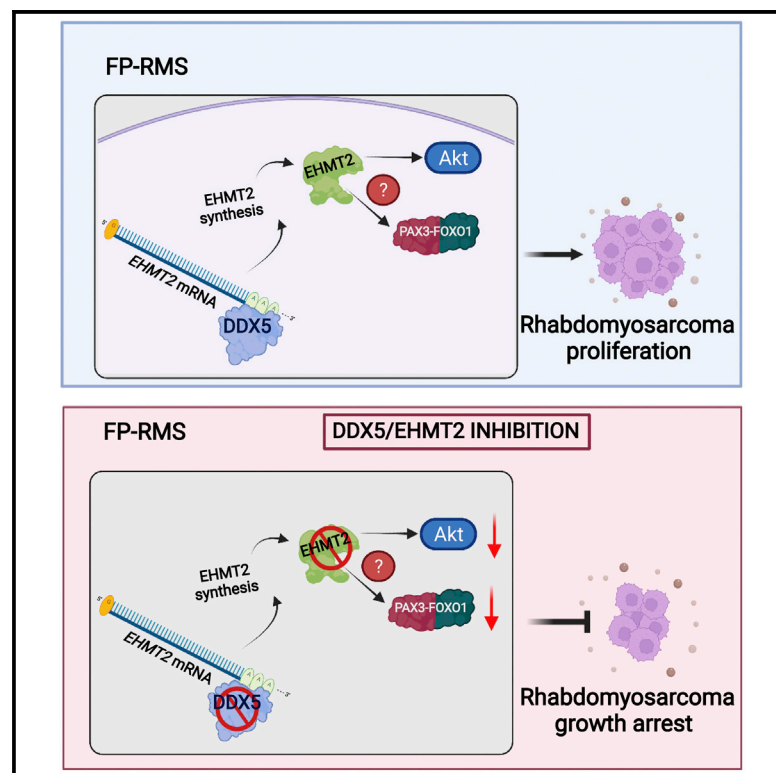# The RNA helicase DDX5 cooperates with EHMT2 to sustain alveolar rhabdomyosarcoma growth

Graphical abstract

Authors

Alberto Gualtieri, Valeria Bianconi, Alessandra Renzini, Luisa Pieroni, Valerio Licursi, Chiara Mozzetta

Correspondence

chiara.mozzetta@uniroma1.it

In brief

Alveolar fusion-positive rhabdomyosarcoma (FP-RMS) is an aggressive soft-tissue sarcoma with a poor clinical outcome and lack of effective targeted treatments. Here, Gualtieri et al. demonstrate that inhibition of DDX5 arrests FP-RMS growth by blocking the pro-survival EHMT2/PAX3-FOXO1 axis that sustains the myoblastic stage.

Highlights

- The RNA helicase DDX5 promotes alveolar rhabdomyosarcoma survival and growth

- DDX5 promotes AKT pathway by directly regulating EHMT2 expression

- DDX5 controls *EHMT2* mRNA stability and protein expression

- EHMT2 interacts with PAX3-FOXO1 modulating its stability in a methylation dependent way

Cell Reports

Report

The RNA helicase DDX5 cooperates with EHMT2 to sustain alveolar rhabdomyosarcoma growth

Alberto Gualtieri,[1,4] Valeria Bianconi,[1,4] Alessandra Renzini,[2,3] Luisa Pieroni,[3] Valerio Licursi,[1] and Chiara Mozzetta[1,5,*]

[1]Institute of Molecular Biology and Pathology (IBPM), National Research Council (CNR) of Italy c/o Department of Biology and Biotechnology "C. Darwin", Sapienza University, 00185 Rome, Italy
[2]Unit of Histology and Medical Embryology, Department of Anatomy, Histology, Forensic Medicine and Orthopedics, Sapienza University, 00185 Rome, Italy
[3]Department of Experimental Neuroscience, Proteomics and Metabolomics Unit, Fondazione Santa Lucia-IRCCS, 00143 Rome, Italy
[4]These authors contributed equally
[5]Lead contact
*Correspondence: chiara.mozzetta@uniroma1.it
https://doi.org/10.1016/j.celrep.2022.111267

SUMMARY

Rhabdomyosarcoma (RMS) is the most common soft-tissue sarcoma of childhood characterized by the inability to exit the proliferative myoblast-like stage. The alveolar fusion positive subtype (FP-RMS) is the most aggressive and is mainly caused by the expression of PAX3/7-FOXO1 oncoproteins, which are challenging pharmacological targets. Here, we show that the DEAD box RNA helicase 5 (DDX5) is overexpressed in alveolar RMS cells and that its depletion and pharmacological inhibition decrease FP-RMS viability and slow tumor growth in xenograft models. Mechanistically, we provide evidence that DDX5 functions upstream of the EHMT2/AKT survival signaling pathway, by directly interacting with *EHMT2* mRNA, modulating its stability and consequent protein expression. We show that EHMT2 in turns regulates PAX3-FOXO1 activity in a methylation-dependent manner, thus sustaining FP-RMS myoblastic state. Together, our findings identify another survival-promoting loop in FP-RMS and highlight DDX5 as a potential therapeutic target to arrest RMS growth.

INTRODUCTION

Rhabdomyosarcomas (RMS) are aggressive cancers representing the most common soft-tissue sarcomas in pediatric population. Most patients diagnosed with RMS are cured by multimodal therapies, including surgery, radiation, and conventional chemotherapeutic drugs. However, clinical outcomes for high-risk RMS patients are still poor, emphasizing the urgency to devise new effective therapeutic interventions (Hettmer et al., 2014).

Pediatric RMS are typically divided into two main categories: alveolar (ARMS) and embryonal (ERMS), which are clinically and molecularly different. ERMS are more common, histologically resemble embryonic skeletal muscle, arise early in childhood from head, neck, and retroperitoneum, and are typically associated with better prognosis. ERMS have a heterogeneous genetic profile associated with activation of tumor-promoting signaling pathways and/or loss of tumor surveillance. ARMS are most common in older children, predominantly involve trunk and extremities, and are generally more aggressive. They typically associate with pathognomonic t(2;13) or t(1;13) chromosomal translocations that result in fusion proteins combining the DNA binding domain of PAX3 or PAX7 with the transcriptional activation domain of FOXO1A, which accounts for 60% or 20% ARMS cases, respectively. The remaining 20% of ARMS lack molecular evidence of these translocations

and are referred to as fusion-negative ARMS (El Demellawy et al., 2017).

Alveolar fusion-positive RMS (FP-RMS) is the most aggressive subtype, associated with frequent metastasis at the time of diagnosis and limited response to treatment, resulting in poor survival rates. FP-RMS cells are addicted to the oncogenic capacity of PAX3/7-FOXO1, which have become key prognostic markers in the clinics. However, direct targeting of the fusion proteins is still a challenge (Wachtel and Schafer, 2018) and other therapeutic vulnerabilities resulting from gene expression changes are being extensively investigated (Seki et al., 2015; Kohsaka et al., 2014; Shern et al., 2014; Gryder et al., 2017). In this context, DEAD box RNA helicases appear appealing candidates as potential therapeutic targets, having been implicated in almost every aspect of RNA metabolism, including transcription, pre-mRNA splicing, ribosome biogenesis, transport, translation, and RNA decay (Linder and Jankowsky, 2011).

In normal myogenesis, the DEAD box helicase 5 (DDX5, also known as p68) is needed for proper differentiation, being part of a multitasking complex that, together with the steroid nuclear receptor activator long non-coding RNA (*SRA*), BRG1 and MYOD, promotes transcriptional expression of MYOD target genes (Caretti et al., 2006). Moreover, DDX5 cooperates with heterogeneous nuclear ribonucleoprotein to establish specific splicing subprograms in myoblasts along myogenesis
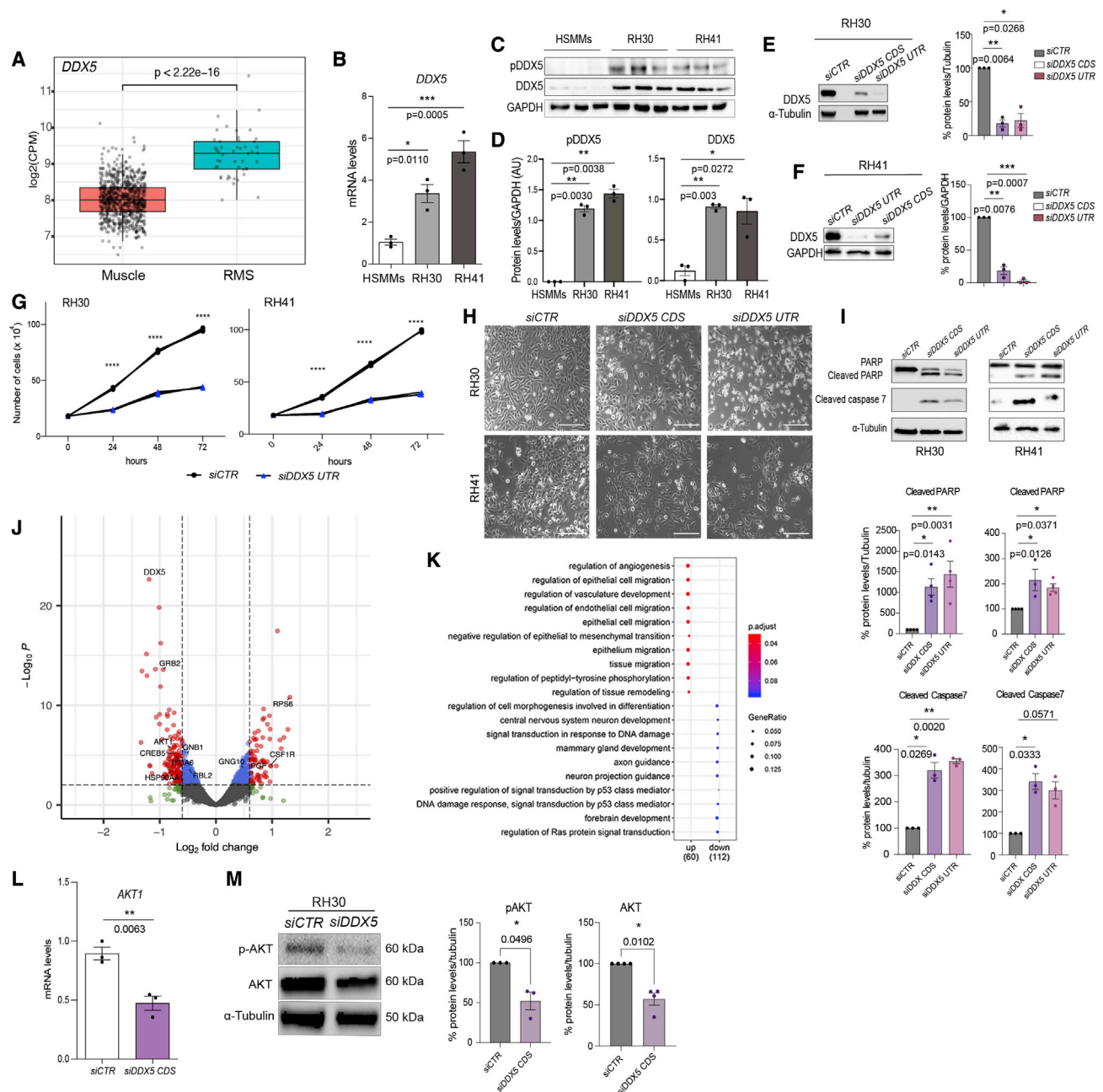
Figure 1. DDX5 promotes FP-RMS growth by regulating AKT signaling

(A) Boxplot of DDX5 mRNA expression levels in RMS biopsies (Chen et al., 2013) and normal human muscle biopsies from GTEx v8 (Gencode v26 annotation).

(B) Relative mRNA expression levels of DDX5 in RH30, RH41, and human skeletal muscle myoblasts (HSMMs).

(C) Representative WB analysis for DDX5 and its phosphorylated form (pDDX5) in RH30, RH41, and HSMMs. GAPDH, loading control.

(D) Quantification of DDX5 and pDDX5 protein levels shown in (C), as a ratio of GAPDH.

(E and F) WB analysis for DDX5 in RH30 (E) and RH41 (F) cells treated with *siCTR*, and *siDDX5* CDS and UTR. Normalization with α-tubulin and GAPDH. Right: quantification of DDX5 levels as a ratio of the corresponding normalizer protein. Levels in *siDDX5* are expressed as percent of *siCTR* (100%).

(G) Growth curves in *siCTR* and *siDDX5* RH30 (left) and RH41 (right) from n = 3 biological replicates.

(H) Representative phase contrast images of RH30 (upper) and RH41 (bottom) 3 days after *siDDX5* and *siCTR*. Scale bar, 100 μm.

(I) WB for apoptotic markers on RH30 (left) and RH41 (right) after *siDDX5* and *siCTR*. α-Tubulin, loading control. Bottom: quantification of the corresponding WB, expressed as percent of the levels in *siCTR*.

(J) Volcano plot of all differentially expressed genes (DEGs), FC > 1.5 e, p_{adj} < 0.05. Genes belonging to "regulation of Ras protein signal transduction" are highlighted on the plot.

(legend continued on next page)

Cell Reports
Report

CellPress
OPEN ACCESS

(Dardenne et al., 2014), highlighting its multimodal actions in shaping cell-specific gene expression programs. Many studies have detected the overexpression of DDX5 in human malignancies and confirmed its involvement in tumorigenesis, invasion, proliferation, and metastasis (Yang et al., 2005; Shin et al., 2007; Nyamao et al., 2019). Thus, DDX5 is a potentially valuable diagnostic and prognostic marker in cancer. However, whether DDX5 plays a role in RMS pathogenesis has been not addressed yet. Here, we demonstrate that DDX5 is overexpressed in FP-RMS and that it promotes its survival and growth, both *in vitro* and *in vivo*. Mechanistically, we found that DDX5 interacts and cooperates with the lysine methyltransferase EHMT2 to stabilize PAX3-FOXO1, thus sustaining the myoblastic stage of FP-RMS.

RESULTS

DDX5 promotes FP-RMS growth by regulating AKT signaling

To gain insights into a role of DDX5 in RMS, we analyzed the Integrated Rhabdomyosarcoma database of the St. Jude Children's Research Hospital (Chen et al., 2013) and verified that its mRNA levels are significantly upregulated in primary RMS compared with normal (muscle) biopsies (Figures 1A and S1A). This evidence is also confirmed by the analysis of patient-derived xenografts (Stewart et al., 2018) indicating a significant upregulation of DDX5 protein in all tested RMS samples (Figure S1B, red bars) and a hyperphosphorylated status compared with normal myoblasts (Figure S1B, circles). Considering the higher *DDX5* RNA levels in alveolar RMS samples (Figure S1A), we focused our further analyses on FP-RMS.

We assessed by quantitative real-time PCR (Figure 1B) and western blot (WB) (Figures 1C and 1D) DDX5 overexpression and its phosphorylation on two different FP-RMS cell lines, RH30 and RH41, compared with normal human skeletal muscle myoblasts (HSMMs). To investigate its functional role, we then inhibited *DDX5* expression in FP-RMS cells through small interfering RNA (siRNA)-mediated knockdown (KD). RH30 and RH41 cells were transfected with two different siRNAs, against DDX5 coding sequence (CDS) and its 3′ untranslated regions (UTRs), which efficiently depleted its expression in the two cell lines compared with cells treated with scramble siRNAs as control (siCTR) (Figures 1E and 1F). DDX5 downregulation significantly reduced FP-RMS growth compared with siCTR cells (Figures 1G and 1H) and WB analysis for the apoptotic markers cleaved PARP and cleaved caspase-7 (Figure 1I), clearly demonstrating the induction of programmed cell death in FP-RMS upon DDX5 silencing. Importantly, this effect was specific for FP-RMS since depletion of DDX5 in HSMMs (Figure S1C) did not arrest cell growth, and neither induced their death (Figure S1D). By

contrast, DDX5 depletion reduced the levels of myogenin in HSMMs (Figure S1C), in line with its pro-differentiative role in normal myogenesis (Caretti et al., 2006; Dardenne et al., 2014).

In light of the evidence that DDX5 is hyperphosphorylated in RMS (Figures 1C, 1D, and S1B) and that pharmacological strategies inhibiting its phosphorylated form (p-DDX5) have proved effective as anti-cancer treatment in a variety of solid tumors (Nyamao et al., 2019), we tested the effect of RX-5902, an inhibitor of p-DDX5 (Yang et al., 2006; Kost et al., 2015), in FP-RMS growth *in vitro* compared with HSMMs. The attenuation of nuclear shuttling of β-catenin being the main effect of RX-5902 (Yang et al., 2006; Kost et al., 2015; Capasso et al., 2019), we assessed target engagement by confirming a decreased nuclear accumulation of β-catenin in RX-5902-treated cells compared with those treated with DMSO (Figure S1E). RX-5902 drastically arrested the growth of both RH30 and RH41 in a concentration-dependent manner (Figures S1F and S1G), inducing their apoptosis (Figure S1H). Notably, no effect was observed in HSMMs, except for a slight decrease at the highest concentration (50 nM) (Figures S1F and S1G), indicating the specific vulnerability of RMS cells to inhibition of pDDX5.

To gain insights into the mechanism behind the role of DDX5 in sustaining FP-RMS growth, we performed transcriptional profiling by RNA-seq in *siDDX5* RH30 compared with *siCTR* cells (Figure 1J). Enrichment analysis of the differentially expressed genes (p < 0.05, FC > 1.5) found "regulation of RAS protein signal transduction" among the top downregulated transcripts (Figure 1K). This evidence caught our attention, as the RAS pathway is aberrantly activated in both FN-RMS and FP-RMS (Skapek et al., 2019). Its predominant downstream signaling pathways, such as the RAF-MEK (mitogen-activated protein kinase-extracellular signal-regulated kinase), and the phosphatidylinositol 3-kinase [PI3K]-AKT-mammalian target of rapamycin), are key to maintain cell growth and proliferation, which is why their inhibition is being tested to arrest cancer cell survival (Cox et al., 2014), with positive effects reported also in RMS (Yohe et al., 2018). Of note, KEGG analysis of the "RAS signaling" pathway (Figure S1I, left) indicated that, among its downstream cascades, "Akt signaling" was the most affected by DDX5 depletion. KEGG on the specific "PI3K-Akt signaling" pathway highlighted downregulation of *AKT1* (Figure S1I, right) and quantitative real-time PCR validated a significant reduction of *AKT1* mRNA levels after *siDDX5* treatment (Figure 1L). Furthermore, we demonstrated that *DDX5* silencing induced a significant reduction of AKT protein levels and, consequently, of the fully activated phosphorylated form of the kinase (p-AKT) (Figure 1M). These data agree with recent work demonstrating that DDX5 promotes hepatocellular carcinoma cell growth via the AKT pathway (Xue et al., 2018), supporting a similar role for DDX5 in sustaining FP-RMS growth and survival.

(K) Dot plot for up- and down-regulated GO terms of biological processes. The size of the dot is based on DEG counts that belong to the pathway, and the color of the dot shows the pathway enrichment significance.

(L) Quantitative real-time PCR for *AKT1* in *siCTR* and *siDDX5* RH30.

(M) WB of p-AKT and AKT in *siCTR* and *siDDX5* RH30. Normalization with α-tubulin. Right: quantification of the corresponding proteins (as a ratio of tubulin levels) expressed as percent of the levels in *siCTR*. Histograms represent mean ± SEM from n = 3 biological replicates. Statistical significance was assessed in (B, D–F, and I) by one-way ANOVA with Bonferroni multiple comparisons test, in (L and M) by an unpaired Student's t test (p values are shown on the graphs), (G) with two-way ANOVA with Sidak's multiple comparison test, ****p < 0.0001. See also Figure S1.

(legend on next page)

Cell Reports
Report

CellPress
OPEN ACCESS
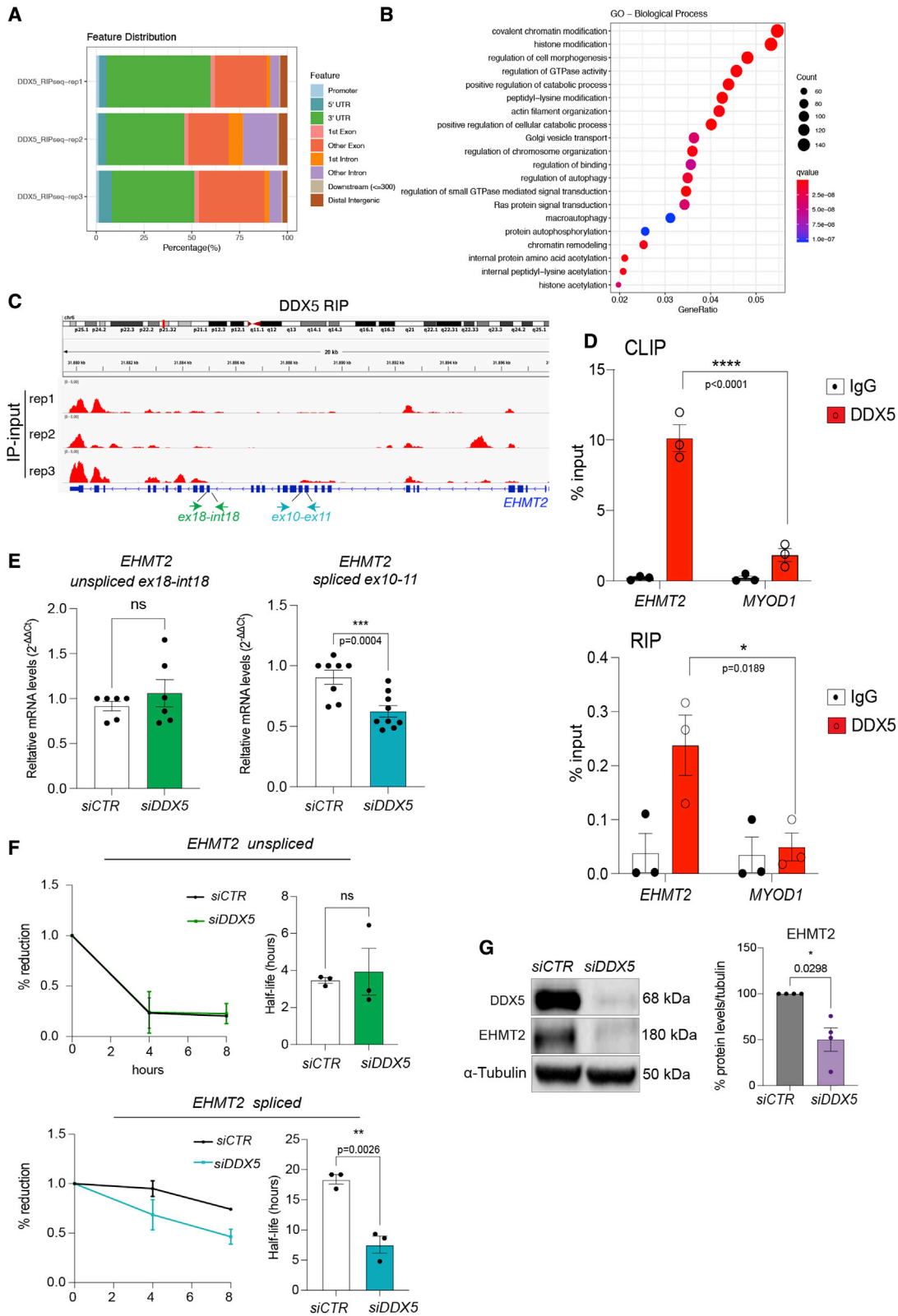
DDX5 interacts with *EHMT2* stabilizing its protein expression

To gain mechanistic insights into DDX5 function in FP-RMS, we mapped the RNAs directly bound by DDX5 in RH30 by performing RNA immunoprecipitation followed by next-generation sequencing (RIP-seq). We found DDX5 mostly associated to 3′ UTR of the immunoprecipitated transcripts (Figure 2A). Gene ontology analysis of the DDX5-bound RNAs revealed that transcripts encoding for chromatin regulators and histone modifiers were among the top enriched categories (Figure 2B; Table S1). These classes were also enriched among the top pathways to which DDX5-bound RNAs belonged (Figure S2A). Within these groups, the transcript encoding for the H3K9 lysine methyltransferase *EHMT2* (Figure 2C) caught our attention because it was recently shown to pathogenically activate AKT signaling by repressing PTEN (Bhat et al., 2019). RIP- and CLIP-qPCR (Figure 2D) confirmed *EHMT2* enrichment in the DDX5 immunoprecipitation (IP) compared with *MYOD1*, which was used as negative control. This evidence led us to hypothesize that DDX5 might promote the AKT pathway (Figures 1K–1M) by directly regulating EHMT2 expression, presumably controlling its RNA at some step of its life cycle. Indeed, DDX5 has been reported to influence the alternative splicing of *EHMT2* (Legrand et al., 2019; Dardenne et al., 2012), a mechanism that affects the stability of the two EHMT2 isoforms (Fiszbein et al., 2016). However, under our conditions, we did not observe any splicing switch among the short and long *EHMT2* isoforms (Figure S2B). Assessment of the expression of all NCBI-annotated *EHMT2* transcripts in our RNA-seq dataset performed in *siCTR* and *siDDX5* cells did not reveal any significant change in their proportion other than the most prevalent one (GenBank: NM_006709) (Figure S2C), pointing against a role for DDX5 in affecting EHMT2 alternative splicing.

To discriminate if DDX5 regulates *EHMT2* transcriptionally or post-transcriptionally, we assessed the levels of unspliced and spliced *EHMT2* mRNA. We found that the expression of the unspliced *EHMT2* transcript was unaffected (Figure 2E, left). By contrast, the spliced form significantly decreased upon *siDDX5* (Figure 2E, right). This result indicates that DDX5 does not directly regulate transcription of *EHMT2* pre-mRNA and rather led us to hypothesize a post-transcriptional control, presumably by promoting mRNA stability. To test this idea, we verified the levels of both spliced and unspliced *EHMT2* after inhibition of transcription by α-amanitin in *siCTR* and *siDDX5* cells (Figure 2F). The drastic decrease of *unspliced EHMT2* confirmed the efficient inhibition of transcription and a rather short half-life of the un-

spliced transcript that was not affected by DDX5 (Figure 2F, upper). By contrast, depletion of DDX5 resulted in a decreased stability of the spliced EHMT2 transcript, which showed a halved half-life compared with control cells (Figure 2F, bottom). Of note, the impaired stability of *EHMT2* RNA, induced by the absence of DDX5, culminates in a significant reduction of EHMT2 protein in FP-RMS cells (Figure 2G).

Together, these results indicate that DDX5 influences EHMT2 expression post-transcriptionally, likely stabilizing the mature transcript and ultimately EHMT2 protein levels.

## DDX5-mediated EHMT2 regulation controls PAX3-FOXO1 expression

FP-RMS are addicted to the oncogenic capacity of PAX3-FOXO1, which perpetuates the myoblastic proliferative state of RMS cells (Gryder et al., 2017). We speculated that DDX5, EHMT2, and PAX3-FOXO1 might be part of a common pro-survival-promoting axis in FP-RMS cells. In support of this, we found that DDX5, EHMT2, and PAX3-FOXO1 physically interacted, in an RNA-dependent manner. Indeed, treatment with RNase A (Figure S3A) decreased the amount of EHMT2 and PAX3-FOXO1 in the IP of DDX5 (Figure 3A). Lack of detected interaction with EZH2, a histone methyltransferase overexpressed in RMS and involved in RMS survival (Ciarapica et al., 2014a, 2014b), confirmed the specificity of EHMT2-DDX5-PAX3FOXO1 interaction under our conditions. Then, we investigated whether DDX5 and/or EHMT2 could have a role in PAX3-FOXO1 modulation. Depletion of both *DDX5* (Figure 3B) and *EHMT2* (Figure 3C) caused a marked reduction of PAX3-FOXO1 protein, but not of its mRNA (Figure S3B), pointing toward a post-transcriptional regulation. Since PAX3-FOXO1 decreased also upon EHMT2 depletion, a condition in which DDX5 levels do not change (Figure 3C), we hypothesized EHMT2 as the major regulator of PAX3-FOXO1 oncoprotein in this axis.

To verify this, we overexpressed a FLAG-tagged form of PAX3-FOXO1 in RH30 stably expressing a Tet-ON inducible *shEHMT2*. Also in this system, EHMT2 depletion, induced by doxycycline (+doxy), led to a significant downregulation of the exogenous FLAG-PAX3-FOXO1 (Figure 3D), further supporting a role for EHMT2 in modulating its expression.

Since pharmacological inhibition of EHMT2, by two specific small-molecule inhibitors, A366 (Figure 3E) and UNC0642 (Figure 3F), exerted similar effects on PAX3-FOXO1 levels, we hypothesized that EHMT2 regulates its expression via enzymatic activity. To support this idea, we assessed the expression levels

---

Figure 2. DDX5 controls *EHMT2* mRNA stability and expression

(A) Genomic region distribution of the RNAs bound by DDX5 assessed by RIP-seq on RH30 (n = 3).

(B) Dot plot of the top 20 most enriched GO biological processes among the DDX5-bound RNAs.

(C) Genome tracks of input-normalized DDX5 RIP-seq in RH30 (n = 3) showing enrichment of *EHMT2*.

(D) Quantitative real-time PCR for *EHMT2* and *MYOD1* on DDX5 CLIPs (upper) and RIPs (bottom). Enrichment shown as % input. RNAs from IgG IP used as negative control.

(E) Quantitative real-time PCR for unspliced (left) and spliced (right) *EHMT2* in *siCTR* and *siDDX5* RH30 cells. Primers for unspliced (green arrows) and the spliced form (blue arrows) are shown in (C).

(F) Left: percent of reduction (from t0) of unspliced (upper) and spliced (bottom) *EHMT2* assessed by quantitative real-time PCR in *siCTR* and *siDDX5* RH30 treated with α-amanitin. Right: RNA half-life calculated on quantitative real-time PCR levels (left), as described in Chen et al. (2008).

(G) WB for EHMT2, DDX5, and tubulin in *siCTR* and *siDDX5* RH30. Right: quantification of EHMT2 protein levels, normalized as a ratio of tubulin, expressed as percent of levels in *siCTR*. Graphs show the mean ± SEM from n = 3 (D and F), 4 (G), or 6 (E) independent experiments. Statistics by unpaired (E and F) or paired (G) t test, and two-way ANOVA with Sidak's multiple comparison test (D). See also Figure S2 and Table S1.
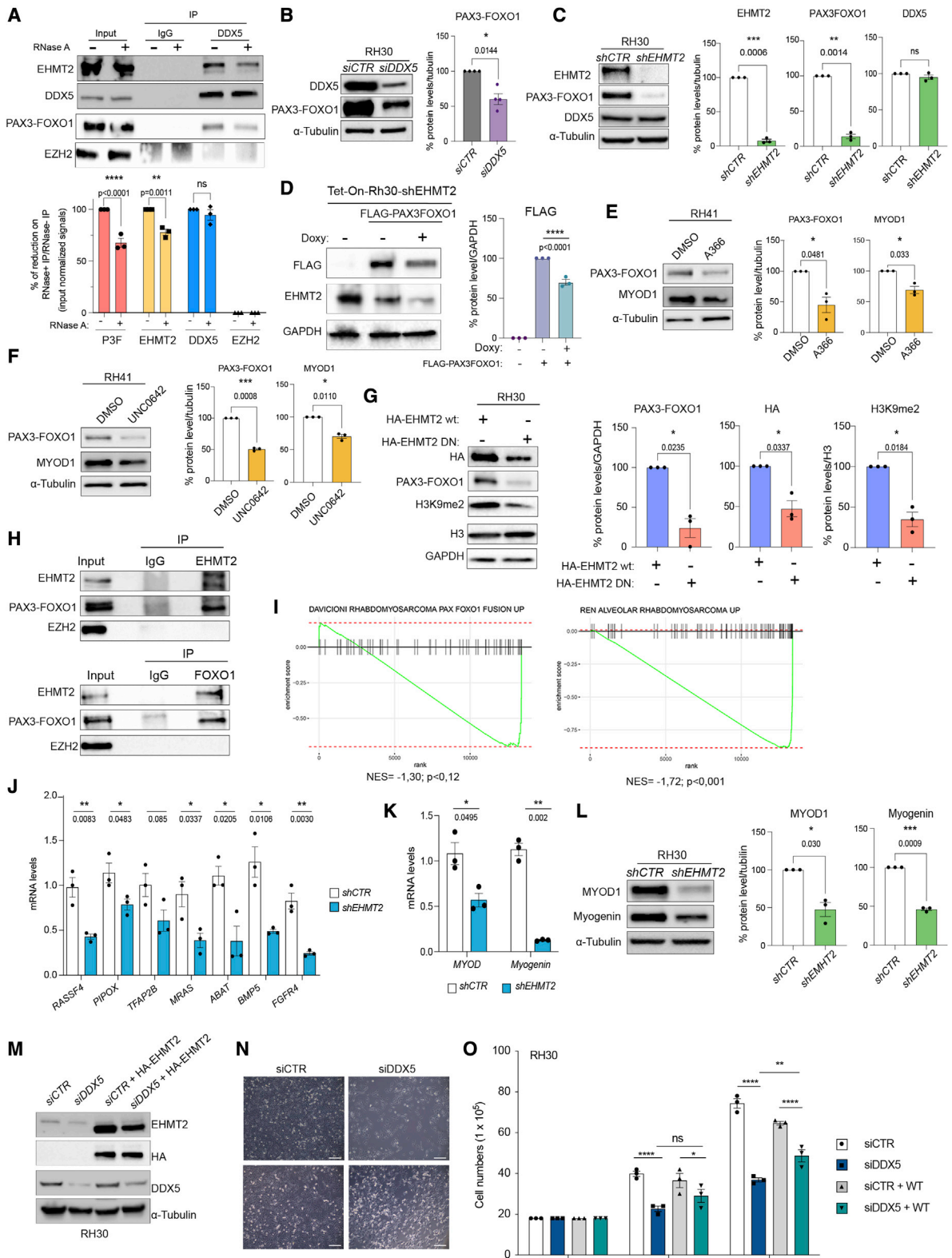
(legend on next page)

of endogenous PAX3-FOXO1 after either expression of a wild-type (WT) HA-tagged form of EHMT2 or a dominant negative catalytically inactive mutant (EHMT2 DN; Gyory et al., 2004) in RH30 cells (Figure 3G). Although the EHMT2 DN mutant was less expressed than EHMT2-WT, as reported (Gyory et al., 2004) and shown by HA levels, it did lead to reduction of PAX3FOXO1, acting as a dominant negative, as demonstrated by the decreased amount of H3K9me2 compared with those observed in EHMT2 WT-expressing cells (Figure 3G). We validated this result also in HeLa cells, showing that the catalytically inactive HA-EHMT2-DN mutant led to a reduction of FLAG-PAX3-FOXO1 levels compared with cells expressing HA-EHMT2-WT (Figure S3C). Together, these results clearly indicate that the enzymatic activity of EHMT2 is important to sustain PAX3-FOXO1 expression.

EHMT2 has a well-known role in methylating non-histone proteins (Mozzetta et al., 2015), and lysine methylation can promote protein stability (Cornett et al., 2019). Thus, we speculated that EHMT2 might stabilize PAX3-FOXO1 through direct methylation. Reciprocal co-immunoprecipitation (coIP) assays further demonstrated that EHMT2 physically interacted with PAX3-FOXO1 (Figures 3H and S3D). However, mass spectrometry analysis of immunoprecipitated FLAG-PAX3-FOXO1 from RH30 by LC-MS did not detect methylated lysine residues (data not shown), pointing toward an indirect yet EHMT2 activity-dependent mechanism promoting PAX3-FOXO1 expression.

Accordingly, transcriptomic analysis of EHMT2-depleted FP-RMS cells (Figure S3E) revealed transcriptional changes inversely correlated by those imposed by PAX3-FOXO1 expression (Ren et al., 2008; Davicioni et al., 2006) (Figures 3I and 3J). Transcript levels of known PAX3-FOXO1 target genes were indeed reduced in EHMT2-depleted cells (Figure 3J).

It has been previously shown that PAX3-FOXO1 activates the RMS master transcription factors MYOD1 and myogenin, and together they establish the transcriptional signatures of FP-RMS (Gryder et al., 2017). Importantly, EHMT2 downregulation (Figures 3K and 3L) and pharmacological inhibition (Figures 3E and 3F) was sufficient to induce a strong reduction of MYOD1 and myogenin expression, both at the RNA (Figure 3K) and protein (Figures 3E, 3F, and 3L) levels. This was confirmed by GSEA, which revealed a significant negative correlation (NES < 0) of transcripts belonging to the "myogenesis" hallmark in EHMT2-depleted cells (Figure S3F) compared with controls, strongly indicating that EHMT2 activity promotes the PAX3-FOXO1-induced myoblastic RMS stage.

In sum, our results reveal the existence of a regulatory axis in which DDX5 functions upstream of EHMT2 and PAX3-FOXO1 to sustain FP-RMS growth, at least in part, by modulating the PI3K-AKT pro-survival pathway. In support of this epistatic relationship, we found the PI3K-AKT cascade among the significantly affected pathways to which genes commonly deregulated in DDX5- or EHMT2-depleted cells belonged (Figures S3G and S3H). Accordingly, EHMT2 downregulation in FP-RMS cells phenocopied the effects imposed by the downregulation of DDX5, such as induction of growth arrest (Figures S3I and S3J) and apoptosis (Figures S3K and S3L); while the rescue of EHMT2 expression in DDX5-depleted cells (Figure 3M) restored their growth (Figures 3N and 3O).

DDX5 promotes FP-RMS growth *in vivo*
Finally, to unequivocally demonstrate a role of DDX5 in mediating FP-RMS tumorigenesis *in vivo*, we performed xenografts experiments by subcutaneously injecting control (shCTR) and DDX5-depleted RH30 cells (shDDX5) into the flanks of BALB/c nude mice. Consistent with our *in vitro* data, tumors derived from shDDX5 displayed a significantly reduced growth over time compared with those derived from control cells (Figure 4A); and excised tumors were much smaller than controls (Figure 4B). Immunohistological analysis showed a significant reduction of proliferating (Ki67+) cells in shDDX5-derived tumors compared

Figure 3. EHMT2 regulates PAX3-FOXO1

(A) Representative WB for the indicated proteins on immunoprecipitation (IP) of DDX5 on RH30 nuclei extracts treated (+) or not (−) with RNAse A. IgG IP used as negative control. Bottom: quantification of the percent of reduction of the IP signal (normalized for the corresponding input; by densitometry analysis) in RNase+ samples compared with the corresponding RNase sample (100%).

(B) Representative WB (left) and quantification (right) for PAX3-FOXO1 in *siCTR* and *siDDX5* RH30. α-Tubulin, loading control.

(C) WB (left) and quantification (right) in *shCTR* and *shEHMT2* RH30 for the indicated proteins.

(D) Representative WB of the indicated proteins (left), and corresponding quantification (right), in RH30 stably expressing a Tet-ON inducible *shEHMT2*, either subjected (+doxy) or not (−doxy) to doxycycline treatment and transfected with equal amounts of FLAG-tagged PAX3-FOXO1 compared with mock control cells.

(E and F) PAX3-FOXO1 WB in RH41 treated with 10 μM A366 (E) and 2 μM UNC0642 (F) for 6 days. Control cells were treated with DMSO and all samples were normalized with α-tubulin. Right: quantification of PAX3-FOXO1 and MYOD1 levels as a ratio of tubulin.

(G) WB of the indicated proteins (left panel) and relative quantification (right) in RH30 transfected with wild-type HA-tagged EHMT2 (HA-EHMT2-WT) or a catalytically inactive dominant negative (DN) EHMT2 (HA-EHMT2-DN).

(H) WB of EHMT2 (upper) and PAX3-FOXO1 (bottom) IP in RH30. IgG was used as a negative control. EZH2 is shown as a negative control of interaction. Input are shown on the left.

(I) GSEA of RNA-seq performed in *shCTR* and shEHMT2 RH41 on two datasets Davicioni et al. (2006) (left) and Ren et al. (2008) (right) for PAX3-FOXO1 target genes.

(J) Quantitative real-time PCR of the indicated PAX3-FOXO1 target genes in *shCTR* and *shEHMT2* cells. mRNA levels were normalized to *GAPDH*.

(K) Quantitative real-time PCR for *MYOD1* and *Myogenin* in *shCTR* and *shEHMT2* RH30.

(L) WB of MYOD and myogenin in *shCTR* and *shEHMT2* RH30. α-Tubulin was used for normalization. Right: quantification of the indicated proteins, as a ratio of tubulin.

(M) WB in *siDDX5* or *siCTR* RH30 cells co-transfected (+EHMT2) or not with an HA-tagged EHMT2 cDNA.

(N and O) Representative pictures (N) and count (O) of cells treated as in (M). Scale bar, 100 μm in (N). All graphs show the mean ± SEM from n = 3 biological replicates, or n = 4 (B). Statistical significance has been assessed by paired Student's t test in (B, C, E–G, and J–L); by one-way ANOVA in (D) and two-way ANOVA in (A and O). p values are shown on the graphs. See also Figure S3.
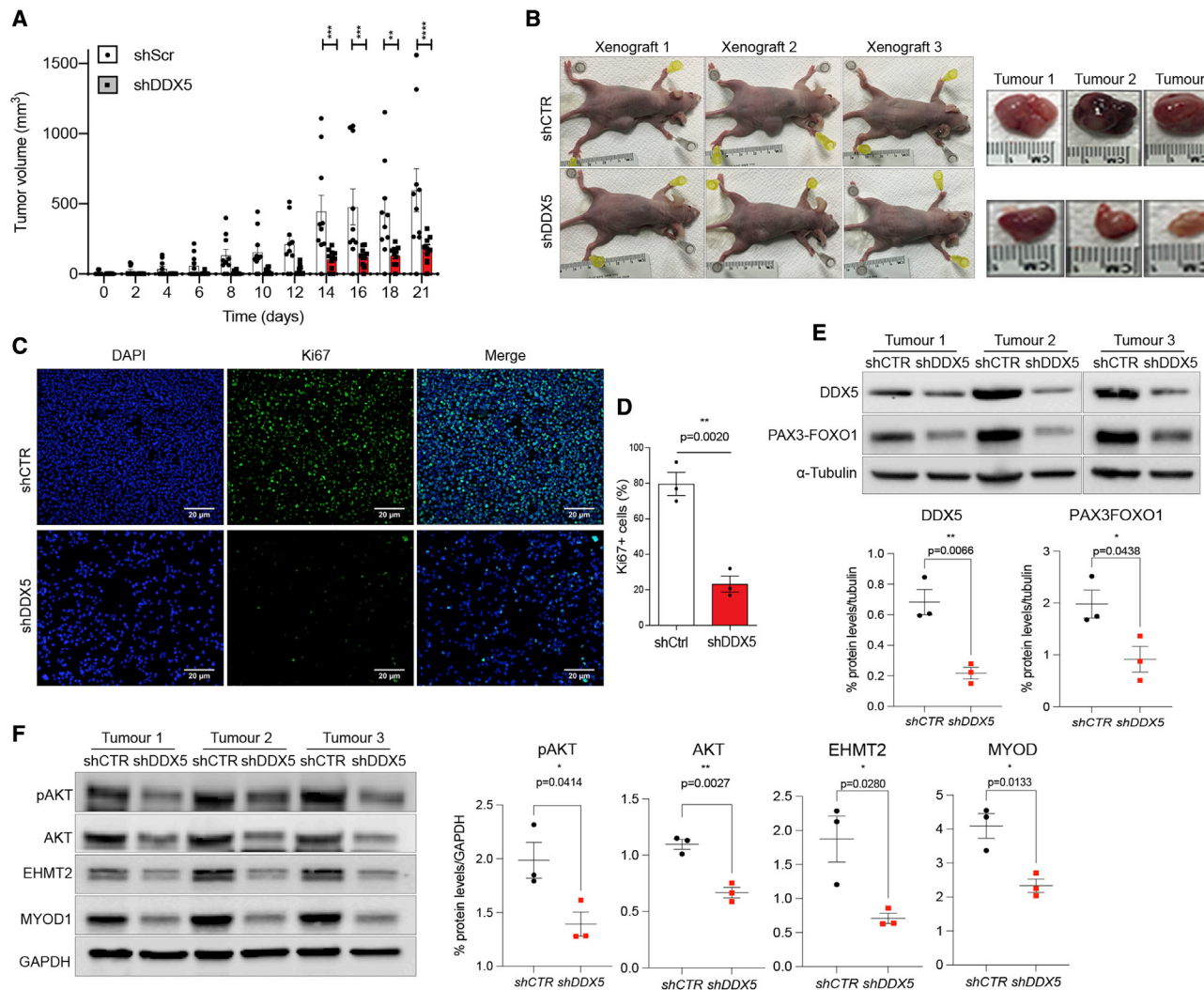
Figure 4. DDX5 promotes FP-RMS growth *in vivo*

(A) Histogram showing the tumor volumes in Balb/c nude subcutaneously inoculated with *shCTR* and *shDDX5* RH30 cells assessed from day of appearance (0) to tumor resection (21).

(B) Representative pictures of n = 3 *shCTR*- and *shDDX5*-treated mice (left) and matching resected tumors (right) at day 21.

(C) Representative images of Ki67 immunostaining (green) on isolated *shCTR* and *shDDX5* tumors. DAPI (blue) was used to stain nuclei. Scale bars, 20 μm.

(D) Percent of Ki67+ cells of the experiment shown in (C).

(E and F) WB for the indicated proteins in tumors derived from *shCTR* and *shDDX5* cells. α-Tubulin and GAPDH, for normalization. Right: quantification of the indicated proteins expressed as ratio of tubulin or GAPDH. Data are shown as mean ± SEM from n = 3 tumors (D–F) or n = 10 mice (A). Statistics by unpaired t test (D–F) or two-way ANOVA, with Sidak's multiple comparison test (A).

with shCTR (Figures 4C and 4D). Furthermore, WB on xenograft-derived proteins confirmed a DDX5-dependent expression of EHMT2 and PAX3-FOXO1 in RMS tumors (Figures 4E and 4F) and that DDX5 downregulation also reduced pAKT, AKT, and MYOD1 protein (Figure 4F) levels, corroborating the role of DDX5 in promoting FP-RMS growth *in vivo*.

DISCUSSION

Like most pediatric cancers, RMS is characterized by a low mutational burden, which limits the ability to risk stratify patients to optimize an efficient multi-layered therapy. Thirty percent of

patients still have poor outcome, and no targeted therapy has entered clinical practice so far (Skapek et al., 2019). Therefore, the identification of new molecular vulnerabilities is critical to accelerate translational progress.

Here, we identified a regulatory axis in FP-RMS that ultimately converges on the modulation of PAX3-FOXO1 expression. We found the RNA helicase DDX5 to be overexpressed in FP-RMS and to regulate the EHMT2/AKT pro-survival signaling (Bhat et al., 2019). We show that EHMT2 directly modulates PAX3-FOXO1 protein levels, suggesting that targeting the DDX5/EHMT2 axis might be an indirect way to block PAX3-FOXO1 oncogenic function.

Cell Reports
Report

CellPress
OPEN ACCESS

EHMT2 has been recently shown to promote the growth of both ARMS and ERMS (Bhat et al., 2019; Pal et al., 2020) via transcriptional modulation of different pathways. In ARMS, EHMT2 directly represses transcription of the tumor suppressor PTEN, thus sustaining activation of the downstream AKT-RAC1 pro-survival signaling (Bhat et al., 2019). By contrast, EHMT2 has been reported to promote ERMS proliferation by recruitment of transcriptional activators on the promoter of the WNT antagonist DKK, thus blocking the pro-differentiative WNT signaling (Pal et al., 2020).

Similarly, EHMT2 has been implicated in sustaining proliferation and expansion of murine muscle stem cells by preventing unscheduled activation of the prodifferentiative WNT signaling cascade through an lncRNA-dependent deposition of H3K9me2 on the WNT7b locus (Cipriano et al., 2021).

Here, we expand this knowledge demonstrating a role for EHMT2 beyond its function as a chromatin modifier. We show that EHMT2 directly interacts with the PAX3-FOXO1 oncoprotein, modulating its stability in a methylation-dependent way. Several chromatin-modifying enzymes have been shown to also modulate PAX3-FOXO1 protein function (Wachtel and Schafer, 2018). EHMT2-dependent lysine methylation of FOXO1 has been involved in degradation rather than stability in colon cancer cells (Chae et al., 2019). However, we did not detect methylation of PAX3-FOXO1 in FP-RMS cells. Although we cannot exclude that this might be due to technical limitations, our evidence favors a model in which EHMT2 indirectly controls PAX3-FOXO1 via regulation of the expression, or stability, of a yet unknown direct regulator.

Our results indicate that DDX5 binds preferentially to RNAs encoding for chromatin regulators, an observation that leads to the speculation that DDX5 might act as a hub modulator of the expression and/or localization of specific classes of transcripts, as reported for other RNA helicases (Zhang et al., 2018). The role of DDX5 in tumorigenesis has long been established (Fuller-Pace, 2013); however, whether it plays a role in promoting RMS proliferation has not been explored so far.

Our results uncover DDX5 as a valuable therapeutic venue to arrest FP-RMS. We demonstrate that its depletion induces FP-RMS to undergo apoptosis, thus blocking the uncontrolled growth both *in vitro* and *in vivo*. From a therapeutic perspective, we show that similar results can be obtained using its pharmacological inhibitor RX-5902 (Yang et al., 2006; Kost et al., 2015). Since RX-5902, a first-in-class orally bioavailable compound, is being tested in clinical trials for different solid tumors (Nyamao et al., 2019), our results might inspire additional studies to test its development in the treatment of RMS patients.

Limitation of the study
The fact that DDX5 downregulation leads to reduced amounts of spliced *EHMT2* mRNA without concurrent accumulation of its unspliced pre-mRNA (Figure 2E) led us to conclude that DDX5 does not affect *EHMT2* transcription per se, but that it is rather involved in a post-transcriptional control of the *EHMT2* life cycle. Considering the well-established role of DDX5 in alternative splicing (Legrand et al., 2019; Dardenne et al., 2012), this result would be compatible with a function of DDX5 in modulating the proportion of EHMT2 isoforms. However, we did not detect

any evident switch among the different annotated *EHMT2* transcripts (Figures S2B and S2C), arguing against this hypothesis. On the other hand, if DDX5 were implicated in conventional splicing, we should have seen an accumulation of the *EHMT2* pre-mRNA upon DDX5 depletion, which is not what we observed in our conditions. As such, we hypothesized that DDX5 is rather involved in the regulation of EHMT2 mRNA stability. This conclusion is supported by the evidence that, upon experimental inhibition of transcription, the half-life of *spliced EHMT2* is halved upon DDX5 depletion, while that of its *unspliced* form is drastically reduced regardless of DDX5 expression (Figure 2F). However, the data presented here do not precisely discriminate the mechanism by which this modulation of RNA stability occurs. Since we found DDX5 enriched at 3′ UTRs of bound RNAs, including *EHMT2* (Figure 2A), it is tempting to speculate that DDX5 might have a role in polyadenylation; however, this needs to be further and properly tested. Moreover, whether this DDX5-dependent control of *EHMT2* expression is mediated by the unwinding enzymatic activity of DDX5 on RNA secondary structure must be additionally investigated.

We also detected a physical, RNA-dependent, interaction between EHMT2, DDX5, and PAX3-FOXO1 (Figure 3A); whether this depends on specific RNAs, such as *EHMT2 mRNA*, must be further tested. The non-interacting protein EZH2 has been used as negative control in our IP experiments (Figures 3A and 3H). However, it should be noted that EZH2 was reported to interact with EHMT2 (Mozzetta et al., 2014) and DDX5 (Zhang et al., 2016) in different cellular contexts. Protein-protein interactions are context- and cell-type specific, and protein dynamics are highly dependent on their environment (Stacey et al., 2018; Federico and Monti, 2021), so it is not surprising that we did not detect EZH2 in our coIP experiments. Nonetheless, we cannot exclude that, in different, less-stringent, conditions EZH2 could be found interacting with these proteins in FP-RMS cells.

Our study also revealed that EHMT2 modulates PAX3-FOXO1 protein levels. By using complementary approaches, we consistently showed that this depends on EHMT2 enzymatic activity. However, we failed to detect direct methylation of PAX3-FOXO1 by LC-MS/MS experiments; or to detect signals for methylated lysines on both endogenous and overexpressed PAX3-FOXO1 immuno-precipitates using pan-K-methyl antibodies. While this could be due to technical limitations, another possibility that we did not address in this study is that EHMT2-mediated regulation of PAX3-FOXO1 might be controlled indirectly through a factor whose expression is dependent on EHMT2 methylation activity.

STAR★METHODS

Detailed methods are provided in the online version of this paper and include the following:

- KEY RESOURCES TABLE
- RESOURCE AVAILABILITY
  - Lead contact
  - Materials availability
  - Data and code availability

AUTHOR CONTRIBUTIONS

A.G. and V.B. performed all the experiments and collected and analyzed data. A.R. and L.P. performed and analyzed LC-MS on FLAG-PAX3-FOXO1 IP. V.L. performed bioinformatic analyses. C.M. conceived, supervised the project, analyzed data, and wrote the manuscript. All authors discussed results and reviewed and edited the manuscript.

DECLARATION OF INTERESTS

The authors declare no competing interests.

INCLUSION AND DIVERSITY

The author list of this paper includes contributors from the location where the research was conducted who participated in the data collection, design, analysis, and/or interpretation of the work.

REFERENCES

Anders, S., Pyl, P.T., and Huber, W. (2015). HTSeq–a Python framework to work with high-throughput sequencing data. Bioinformatics *31*, 166–169.

Ashburner, M., Ball, C.A., Blake, J.A., Botstein, D., Butler, H., Cherry, J.M., Davis, A.P., Dolinski, K., Dwight, S.S., Eppig, J.T., et al. (2000). Gene ontology: tool for the unification of biology. The Gene Ontology Consortium. Nat. Genet. *25*, 25–29.

Bhat, A.V., Palanichamy kala, M., Rao, V.K., Pignata, L., Lim, H.J., Suriyamurthy, S., Chang, K.T., Lee, V.K., Guccione, E., and Taneja, R. (2019). Epigenetic regulation of the PTEN-AKT-RAC1 Axis by G9a is critical for tumor growth in alveolar rhabdomyosarcoma. Cancer Res. *79*, 2232–2243.

Bray, N.L., Pimentel, H., Melsted, P., and Pachter, L. (2016). Near-optimal probabilistic RNA-seq quantification. Nat. Biotechnol. *34*, 525–527.

Capasso, A., Bagby, S.M., Dailey, K.L., Currimjee, N., Yacob, B.W., Ionkina, A., Frank, J.G., Kim, D.J., George, C., Lee, Y.B., et al. (2019). First-in-Class phosphorylated-p68 inhibitor RX-5902 inhibits beta-catenin signaling and demonstrates antitumor activity in triple-negative breast cancer. Mol. Cancer Ther. *18*, 1916–1925.

Caretti, G., Schiltz, R.L., Dilworth, F.J., Di Padova, M., Zhao, P., Ogryzko, V., Fuller-Pace, F.V., Hoffman, E.P., Tapscott, S.J., and Sartorelli, V. (2006). The RNA helicases p68/p72 and the noncoding RNA SRA are coregulators of MyoD and skeletal muscle differentiation. Dev. Cell *11*, 547–560.

Chae, Y.C., Kim, J.Y., Park, J.W., Kim, K.B., Oh, H., Lee, K.H., and Seo, S.B. (2019). FOXO1 degradation via G9a-mediated methylation promotes cell proliferation in colon cancer. Nucleic Acids Res. *47*, 1692–1705.

Chen, C.Y.A., Ezzeddine, N., and Shyu, A.B. (2008). Messenger RNA half-life measurements in mammalian cells. Methods Enzymol. *448*, 335–357.

Chen, X., Stewart, E., Shelat, A.A., Qu, C., Bahrami, A., Hatley, M., Wu, G., Bradley, C., Mcevoy, J., Pappo, A., et al.; St Jude Children's Research Hospital–Washington University Pediatric Cancer Genome Project (2013). Targeting oxidative stress in embryonal rhabdomyosarcoma. Cancer Cell *24*, 710–724.

Ciarapica, R., Carcarino, E., Adesso, L., De Salvo, M., Bracaglia, G., Leoncini, P.P., Dall'Agnese, A., Verginelli, F., Milano, G.M., Boldrini, R., et al. (2014a). Pharmacological inhibition of EZH2 as a promising differentiation therapy in embryonal RMS. BMC Cancer *14*, 139.

Ciarapica, R., De Salvo, M., Carcarino, E., Bracaglia, G., Adesso, L., Leoncini, P.P., Dall'Agnese, A., Walters, Z.S., Verginelli, F., De Sio, L., et al. (2014b). The Polycomb group (PcG) protein EZH2 supports the survival of PAX3-FOXO1 alveolar rhabdomyosarcoma by repressing FBXO32 (Atrogin1/MAFbx). Oncogene *33*, 4173–4184.

Cipriano, A., Macino, M., Buonaiuto, G., Santini, T., Biferali, B., Peruzzi, G., ColantonI, A., Mozzetta, C., and Ballarino, M. (2021). Epigenetic regulation of Wnt7b expression by the cis-acting long noncoding RNA Lnc-Rewind in muscle stem cells. Elife *10*, e54782.

Cornett, E.M., Ferry, L., Defossez, P.A., and RothbarT, S.B. (2019). Lysine methylation regulators moonlighting outside the epigenome. Mol. Cell *75*, 1092–1101.

Cox, A.D., Fesik, S.W., Kimmelman, A.C., Luo, J., and Der, C.J. (2014). Drugging the undruggable RAS: mission possible? Nat. Rev. Drug Discov. *13*, 828–851.

Dardenne, E., Pierredon, S., Driouch, K., Gratadou, L., Lacroix-Triki, M., Espinoza, M.P., Zonta, E., Germann, S., Mortada, H., Villemin, J.P., et al. (2012). Splicing switch of an epigenetic regulator by RNA helicases promotes tumor-cell invasiveness. Nat. Struct. Mol. Biol. *19*, 1139–1146.

Dardenne, E., Polay Espinoza, M., Fattet, L., Germann, S., Lambert, M.P., Neil, H., Zonta, E., Mortada, H., Gratadou, L., Deygas, M., et al. (2014). RNA helicases DDX5 and DDX17 dynamically orchestrate transcription, miRNA, and splicing programs in cell differentiation. Cell Rep. *7*, 1900–1913.

Davicioni, E., Finckenstein, F.G., Shahbazian, V., Buckley, J.D., Triche, T.J., and Anderson, M.J. (2006). Identification of a PAX-FKHR gene expression

Cell Reports
Report

signature that defines molecular classes and determines the prognosis of alveolar rhabdomyosarcomas. Cancer Res. *66*, 6936–6946.

Dobin, A., Davis, C.A., Schlesinger, F., Drenkow, J., Zaleski, C., Jha, S., Batut, P., Chaisson, M., and Gingeras, T.R. (2013). STAR: ultrafast universal RNA-seq aligner. Bioinformatics *29*, 15–21.

El Demellawy, D., Mcgowan-Jordan, J., De Nanassy, J., Chernetsova, E., and Nasr, A. (2017). Update on molecular findings in rhabdomyosarcoma. Pathology *49*, 238–246.

Federico, A., and Monti, S. (2021). Contextualized protein-protein interactions. Patterns (N Y) *2*, 100153.

Fiszbein, A., Giono, L.E., Quaglino, A., Berardino, B.G., Sigaut, L., Von Bilderling, C., Schor, I.E., Steinberg, J.H.E., Rossi, M., Pietrasanta, L.I., et al. (2016). Alternative splicing of G9a regulates neuronal differentiation. Cell Rep. *14*, 2797–2808.

Fuller-Pace, F.V. (2013). DEAD box RNA helicase functions in cancer. RNA Biol. *10*, 121–132.

Gentleman, R.C., Carey, V.J., Bates, D.M., Bolstad, B., Dettling, M., Dudoit, S., Ellis, B., Gautier, L., Ge, Y., Gentry, J., et al. (2004). Bioconductor: open software development for computational biology and bioinformatics. Genome Biol. *5*, R80.

Gryder, B.E., Yohe, M.E., Chou, H.C., Zhang, X., Marques, J., Wachtel, M., Schaefer, B., Sen, N., Song, Y., Gualtieri, A., et al. (2017). PAX3-FOXO1 establishes myogenic super enhancers and confers BET bromodomain vulnerability. Cancer Discov. *7*, 884–899.

Gyory, I., Wu, J., Fejér, G., Seto, E., and Wright, K.L. (2004). PRDI-BF1 recruits the histone H3 methyltransferase G9a in transcriptional silencing. Nat. Immunol. *5*, 299–308.

Hettmer, S., Li, Z., Billin, A.N., Barr, F.G., Cornelison, D.D.W., Ehrlich, A.R., GuttridgE, D.C., Hayes-Jordan, A., Helman, L.J., Houghton, P.J., et al. (2014). Rhabdomyosarcoma: current challenges and their implications for developing therapies. Cold Spring Harb. Perspect. Med. *4*, a025650.

Hinson, A.R.P., Jones, R., Crose, L.E.S., Belyea, B.C., Barr, F.G., and Linardic, C.M. (2013). Human rhabdomyosarcoma cell lines for rhabdomyosarcoma research: utility and pitfalls. Front. Oncol. *3*, 183.

Kohsaka, S., Shukla, N., Ameur, N., Ito, T., Ng, C.K.Y., Wang, L., Lim, D., Marchetti, A., Viale, A., Pirun, M., et al. (2014). A recurrent neomorphic mutation in MYOD1 defines a clinically aggressive subset of embryonal rhabdomyosarcoma associated with PI3K-AKT pathway mutations. Nat. Genet. *46*, 595–600.

Kost, G.C., Yang, M.Y., Li, L., Zhang, Y., Liu, C.Y., Kim, D.J., Ahn, C.H., Lee, Y.B., and Liu, Z.R. (2015). A novel anti-cancer agent, 1-(3, 5-Dimethoxyphenyl)-4-[(6-Fluoro-2-Methoxyquinoxalin-3-yl)Aminocarbonyl] Piperazine (RX-5902), interferes with beta-catenin function through Y593 Phospho-p68 RNA helicase. J. Cell. Biochem. *116*, 1595–1601.

Lawrence, M., Huber, W., Pagès, H., Aboyoun, P., Carlson, M., Gentleman, R., Morgan, M.T., and Carey, V.J. (2013). Software for computing and annotating genomic ranges. PLoS Comput. Biol. *9*, e1003118.

Legrand, J.M.D., Chan, A.L., La, H.M., Rossello, F.J., Änkö, M.L., Fuller-Pace, F.V., and Hobbs, R.M. (2019). DDX5 plays essential transcriptional and post-transcriptional roles in the maintenance and function of spermatogonia. Nat. Commun. *10*, 2278.

Li, H., Handsaker, B., Wysoker, A., Fennell, T., Ruan, J., Homer, N., Marth, G., Abecasis, G., and Durbin, R.; 1000 Genome Project Data Processing Subgroup (2009). The sequence alignment/map format and SAMtools. Bioinformatics *25*, 2078–2079.

Linder, P., and Jankowsky, E. (2011). From unwinding to clamping - the DEAD box RNA helicase family. Nat. Rev. Mol. Cell Biol. *12*, 505–516.

Love, M.I., Huber, W., and Anders, S. (2014). Moderated estimation of fold change and dispersion for RNA-seq data with DESeq2. Genome Biol. *15*, 550.

Martin, M. (2011). Cutadapt removes adapter sequences from high-throughput sequencing reads. EMBnet. J. *17*, 10–12.

Mozzetta, C., Boyarchuk, E., Pontis, J., and Ait-Si-Ali, S. (2015). Sound of silence: the properties and functions of repressive Lys methyltransferases. Nat. Rev. Mol. Cell Biol. *16*, 499–513.

Mozzetta, C., Pontis, J., Fritsch, L., Robin, P., Portoso, M., Proux, C., Margueron, R., and Ait-Si-Ali, S. (2014). The histone H3 lysine 9 methyltransferases G9a and GLP regulate polycomb repressive complex 2-mediated gene silencing. Mol. Cell *53*, 277–289.

Nyamao, R.M., Wu, J., Yu, L., Xiao, X., and Zhang, F.M. (2019). Roles of DDX5 in the tumorigenesis, proliferation, differentiation, metastasis and pathway regulation of human malignancies. Biochim. Biophys. Acta. Rev. Cancer *1871*, 85–98.

Ogata, H., Goto, S., Sato, K., Fujibuchi, W., Bono, H., and Kanehisa, M. (1999). KEGG: Kyoto Encyclopedia of genes and genomes. Nucleic Acids Res. *27*, 29–34.

Pal, A., Leung, J.Y., Ang, G.C.K., Rao, V.K., Pignata, L., Lim, H.J., Hebrard, M., Chang, K.T., Lee, V.K., Guccione, E., and Taneja, R. (2020). EHMT2 epigenetically suppresses Wnt signaling and is a potential target in embryonal rhabdomyosarcoma. Elife *9*, e57683.

Ren, Y.X., Finckenstein, F.G., Abdueva, D.A., Shahbazian, V., Chung, B., Weinberg, K.I., Triche, T.J., Shimada, H., and Anderson, M.J. (2008). Mouse mesenchymal stem cells expressing PAX-FKHR form alveolar rhabdomyosarcomas by cooperating with secondary mutations. Cancer Res. *68*, 6587–6597.

Rinn, J.L., Kertesz, M., Wang, J.K., Squazzo, S.L., Xu, X., Brugmann, S.A., Goodnough, L.H., Helms, J.A., Farnham, P.J., Segal, E., and Chang, H.Y. (2007). Functional demarcation of active and silent chromatin domains in human HOX loci by noncoding RNAs. Cell *129* (7), 1311–1323.

Robinson, M.D., Mccarthy, D.J., and Smyth, G.K. (2010). edgeR: a Bioconductor package for differential expression analysis of digital gene expression data. Bioinformatics *26*, 139–140.

Seki, M., Nishimura, R., Yoshida, K., Shimamura, T., Shiraishi, Y., Sato, Y., Kato, M., Chiba, K., Tanaka, H., Hoshino, N., et al. (2015). Integrated genetic and epigenetic analysis defines novel molecular subgroups in rhabdomyosarcoma. Nat. Commun. *6*, 7557.

Shern, J.F., Chen, L., Chmielecki, J., Wei, J.S., Patidar, R., Rosenberg, M., Ambrogio, L., Auclair, D., Wang, J., Song, Y.K., et al. (2014). Comprehensive genomic analysis of rhabdomyosarcoma reveals a landscape of alterations affecting a common genetic axis in fusion-positive and fusion-negative tumors. Cancer Discov. *4*, 216–231.

Shin, S., Rossow, K.L., Grande, J.P., and Janknecht, R. (2007). Involvement of RNA helicases p68 and p72 in colon cancer. Cancer Res. *67*, 7572–7578.

Skapek, S.X., Ferrari, A., Gupta, A.A., Lupo, P.J., Butler, E., Shipley, J., Barr, F.G., and Hawkins, D.S. (2019). Rhabdomyosarcoma. Nat. Rev. Dis. Primers *5*, 1.

Stacey, R.G., Skinnider, M.A., Chik, J.H.L., and Foster, L.J. (2018). Context-specific interactions in literature-curated protein interaction databases. BMC Genom. *19*, 758.

Stewart, E., Mcevoy, J., Wang, H., Chen, X., Honnell, V., Ocarz, M., Gordon, B., Dapper, J., Blankenship, K., Yang, Y., et al.; St Jude Children's Research Hospital – Washington University Pediatric Cancer Genome Project (2018). Identification of therapeutic targets in rhabdomyosarcoma through integrated genomic, epigenomic, and proteomic analyses. Cancer Cell *34*, 411–426.e19.

Subramanian, A., Tamayo, P., Mootha, V.K., Mukherjee, S., Ebert, B.L., Gillette, M.A., Paulovich, A., Pomeroy, S.L., Golub, T.R., Lander, E.S., and Mesirov, J.P. (2005). Gene set enrichment analysis: a knowledge-based approach for interpreting genome-wide expression profiles. Proc. Natl. Acad. Sci. USA *102*, 15545–15550.

Tu, W.B., Shiah, Y.J., Lourenco, C., Mullen, P.J., Dingar, D., Redel, C., Tamachi, A., Ba-Alawi, W., Aman, A., Al-Awar, R., et al. (2018). MYC interacts with the G9a histone methyltransferase to drive transcriptional repression and tumorigenesis. Cancer Cell *34*, 579–595.e8.

Wachtel, M., and Schafer, B.W. (2018). PAX3-FOXO1: zooming in on an "undruggable" target. Semin. Cancer Biol. *50*, 115–123.

Xue, Y., Jia, X., Li, L., Dong, X., Ling, J., Yuan, J., and Li, Q. (2018). DDX5 promotes hepatocellular carcinoma tumorigenesis via Akt signaling pathway. Biochem. Biophys. Res. Commun. *503*, 2885–2891.

Yang, L., Lin, C., and Liu, Z.R. (2005). Phosphorylations of DEAD box p68 RNA helicase are associated with cancer development and cell proliferation. Mol. Cancer Res. 3, 355–363.

Yang, L., Lin, C., and Liu, Z.R. (2006). P68 RNA helicase mediates PDGF-induced epithelial mesenchymal transition by displacing Axin from beta-catenin. Cell 127, 139–155.

Yohe, M.E., Gryder, B.E., Shern, J.F., Song, Y.K., Chou, H.C., Sindiri, S., Mendoza, A., Patidar, R., Zhang, X., Guha, R., et al. (2018). MEK inhibition induces MYOG and remodels super-enhancers in RAS-driven rhabdomyosarcoma. Sci. Transl. Med. 10, eaan4470.

Yu, G., Wang, L.G., Han, Y., and He, Q.Y. (2012). clusterProfiler: an R package for comparing biological themes among gene clusters. OMICS 16, 284–287.

Zhang, H., Xing, Z., Mani, S.K.K., Bancel, B., Durantel, D., Zoulim, F., Tran, E.J., Merle, P., and Andrisani, O. (2016). RNA helicase DEAD box protein 5 regulates Polycomb repressive complex 2/Hox transcript antisense intergenic RNA function in hepatitis B virus infection and hepatocarcinogenesis. Hepatology 64, 1033–1048.

Zhang, L., Yang, Y., Li, B., Scott, I.C., and Lou, X. (2018). The DEAD-box RNA helicase Ddx39ab is essential for myocyte and lens development in zebrafish. Development 145, dev161018.

Zhang, Y., Liu, T., Meyer, C.A., Eeckhoute, J., Johnson, D.S., Bernstein, B.E., Nusbaum, C., Myers, R.M., Brown, M., Li, W., and Liu, X.S. (2008). Model-based analysis of ChIP-seq (MACS). Genome Biol. 9, R137.

Cell Reports
Report

CellPress
OPEN ACCESS

STAR★METHODS

KEY RESOURCES TABLE

REAGENT or RESOURCE	SOURCE	IDENTIFIER
Antibodies		
DDX5	Cell Signaling	cat#: 9877; RRID:AB_2616008
pDDX5 Tyr593	BIOSS	cat#: bs-8005R; RRID: N/A
EHTM2	Cell Signaling	cat#: 3306; RRID:AB_2097647
FOXO1	Cell Signaling	cat#: 2880; RRID:AB_2106495
p-AKT (Ser473)	Cell Signaling	cat#: 4058; RRID:AB_331168
AKT	Cell Signaling	cat#: 4685; RRID:AB_2225340
PARP	Cell Signaling	cat#: 9542; RRID:AB_2160739
Cleaved caspase 7	Cell Signaling	cat#: 8438; RRID:AB_11178377
Cleaved caspase 9	Cell Signaling	cat#: 9505; RRID:AB_2290727
MYOD c-20	Santa Cruz	cat#: Sc-304; RRID:AB_631992
Myogenin F5D	DSHB	cat#: F5D; RRID:AB_2146602
GAPDH	Sigma-Aldrich	cat#: G9545; RRID:AB_796208
Alpha-tubulin	Sigma-Aldrich	cat#: T5168; RRID:AB_477579
DDX5	Abcam	cat#: Ab10261; RRID:AB_297000
H3K9me2	Abcam	cat#: Ab1220; RRID:AB_449854
LaminB	Abcam	cat#: Ab16048; RRID:AB_443298
KI-67	Abcam	cat#: 15580; RRID:AB_443209
DAPI	Sigma-Aldrich	cat#: D9542
Anti- mouse IgG peroxidase antibody	Sigma-Aldrich	cat#: A9044; RRID:AB_258431
Anti- rabbit IgG peroxidase antibody	Sigma-Aldrich	cat#: A9169; RRID:AB_258434
Alexa fluor 488 secondary antibody	Thermo Fisher	cat#: A21206; RRID:AB_2535792
Normal rabbit IgG	Thermo Fisher	cat#: 10500C; RRID:AB_2532981
Chemicals, peptides, and recombinant proteins		
Dulbecco's modified Eagle's medium (DMEM)	Sigma-Aldrich	cat#: D5671
FBS	Corning	cat#: 35-015-CV
RPMI-1640	Sigma-Aldrich	cat#: R8758
GlutaMAX	GIBCO	cat#: 35050-061
Dulbecco's Phosphate Buffered Saline (PBS)	Sigma-Aldrich	cat#: D8537
Penicillin-Streptomycin	Sigma-Aldrich	cat#: P0781
TRYPSIN-EDTA SOLUTION 0.25%	Sigma-Aldrich	cat#: T4049
Dimethyl Sulfoxide	Sigma-Aldrich	Cat#: D8418
A-366	Sigma-Aldrich	cat#: SML1410
UNC0642	Tocris	cat#: 5132
RX-5902	Chemietek	cat#: CT-RX5902 Lot 01
Lipofectamine 2000	Invitrogen	cat#: 11668019
α-amanitin	Sigma-Aldrich	cat#: A2263
Puromycin	Sigma-Aldrich	cat#: P8833

(Continued on next page)

Continued

REAGENT or RESOURCE	SOURCE	IDENTIFIER
RNase A	Sigma-Aldrich	cat#: R6513
G418	Sigma-Aldrich	cat#: A1720
TRI-reagent	Sigma-Aldrich	cat#: T9424
SYBR green Master Mix	Applied Biosystems	cat#: A25742
4%–20% Mini-PROTEAN TGX gels	Bio Rad	cat#: 4561095
Nitrocellulose membrane Protran 0.45um	Amersham	Cat#: 10600002
SKIM MILK	Sigma-Aldrich	cat#: 70166
TRIZMA	Sigma-Aldrich	cat#: T1503
TWEEN	APPLICHEM	cat#: A1389
Western Bright ECL solution	ADVANSTA	cat#: K120-45 D20
Pierce^{TM} ChIP-grade Protein A/G Magnetic Beads	Thermo Fisher Scientific	cat#: 26162
KCl	Sigma-Aldrich	cat#: P9541
MgCl$_2$	APPLICHEM	cat#: A4425
Sodium chloride NaCl	Sigma-Aldrich	cat#: S3014
EDTA	Sigma-Aldrich	cat#: A1104
EGTA	APPLICHEM	cat#: A0878
NP-40	Sigma-Aldrich	cat#: 74385
GLYCEROL	APPLICHEM	cat#: A2926 0500
Phenylmethanesulfonyl fluoride solution	Sigma-Aldrich	cat#: 93482
Complete protease inhibitors tablets	Roche	cat#: 0-4693116001
Phosphatase Inhibitors PhosSTOP	Roche	cat#: 4906845001
SDS	APPLICHEM	cat#: A2263
Critical commercial assays		
SkGM-2 Bullet Kit	LONZA	cat#: CC-3245
Quick-RNA Miniprep Kit	Zymo Research	cat#: R1055
cDNA high-capacity reverse transcription kit	Applied Biosystems	cat#: 4368814
BCA assay	Thermo Fisher	cat#: 23227
Trio RNA-Seq kit	Tecan Genomics	N/A
QuantSeq 3′mRNA-Seq Library prep kit	Lexogen	N/A
Deposited data		
RNAseq RMS human biopsies	(Chen et al., 2013).	https://platform.stjude.cloud/data/diseases/paired-tumor-normal
RNA-Seq from RMS PDX	(Stewart et al., 2018).	https://pecan.stjude.cloud/proteinpaint/study/RHB2018
RNA-Seq from normal human skeletal muscles	GTEX	http://xena.ucsc.edu/
RNA-Seq data	This paper	GEO: GSE152358 and GEO: GSE152359
DDX5 RIP-Seq data	This paper	GEO: GSE175455
Experimental models: Cell lines		
HSMMs	Sigma-Aldrich	cat#: C-14060
HEK293T cells	Dr. Slimane Ait-Si-Ali lab (CNRS, Université Paris Cité, France)	N/A
RH30 cells	Dr. Rossella Rota lab (Bambino Gesù Children's Hospital, IRCCS, Rome, Italy)	N/A
RH41 cells	Dr. Rossella Rota lab (Bambino Gesù Children's Hospital, IRCCS, Rome, Italy)	N/A

Cell Reports
Report

Continued

REAGENT or RESOURCE	SOURCE	IDENTIFIER
Experimental models: Organisms/strains		
Balb/c nude mice (BALB/cOlaHsd-*Foxn1[nu]*)	Envigo	cat#: 165 - IT
Oligonucleotides		
siDDX5 UTR, Sense: 5′-AACCGCAACCAUUGACGCCAU-3′	Sigma-Aldrich	N/A
siDDX5 UTR, Antisense: 5′-AUGGCGUCAAUGGUUGCGGUU-3′	Sigma-Aldrich	N/A
siDDX5 CDS, Sense: 5′-GGCUAGAUGUGGAAGAUGU-3′	Sigma-Aldrich	N/A
siDDX5 CDS, Antisense: 5′-ACAUCUUCCACAUCUAGCC-3′	Sigma-Aldrich	N/A
siRNA universal negative control	Sigma-Aldrich	cat#: SIC001
For primers sequence for qPCR see Table S2	Sigma-Aldrich	N/A
Recombinant DNA		
shRNA pLKO.1-puro, EHMT2 Mission shRNA	Sigma-Aldrich	TRCN0000115671; GeneBank: NM_025256
DDX5 Mission shRNA plasmid DNA, AACCGCAACCAUUGACGCCAU	Sigma-Aldrich	GeneBank: NM_004396
mission control shRNA plasmid DNA	Sigma-Aldrich	cat#: SHC016
pLKO.1-neo vector encoding for a Tet-On-shEHMT2	(Tu et al., 2018)	Prof. Linda Penn's lab (University of Toronto, Canada)
Software and algorithms		
Prism version 6.0	GraphPad Software Inc.	www.graphpad.com
Adobe Illustrator cc2017	Adobe Systems	www.adobe.com
HTSeq-count version 0.8.0	(Anders et al., 2015)	https://htseq.readthedocs.io/en/release_0.8.0/overview.html
Fast QC	Babraham Institute	https://www.bioinformatics.babraham.ac.uk/projects/
TrimGalore Software	Babraham Institute	https://www.bioinformatics.babraham.ac.uk/projects/trim_galore/
edgeR	(Robinson et al., 2010)	https://bioconductor.org/packages/edgeR
DESeq2	(Love et al., 2014)	https://bioconductor.org/packages/release/bioc/html/DESeq2.html
GenomicRanges	(Lawrence et al., 2013)	https://bioconductor.org/packages/release/bioc/html/GenomicRanges.html
GenomicFeatures	(Lawrence et al., 2013)	https://bioconductor.org/packages/release/bioc/html/GenomicFeatures.html
clusterProfiler	(Yu et al., 2012)	https://bioconductor.org/packages/clusterProfiler
Cutadapt version 1.11	(Martin, 2011)	http://code.google.com/p/cutadapt/.
Samtools	(Li et al., 2009)	http://www.htslib.org/
ZEN 3.0	ZEISS	https://www.zeiss.com
ImageLab	Biorad	https://www.bio-rad.com
Other		
Nanodrop	Nanodrop Technologies	N/A
Step-One plus Real-Time PCR System	Applied Biosystems	N/A
Trans-Blot Turbo Transfer system	Bio-Rad Laboratories	1704150
Illumina NovaSeq6000	Illumina	N/A
Bioruptor Pico & Cooler	Diagenode	Cat#: B01060010
CHEMIDOC	BIORAD	XRS+
MICROSCOPE AXIO OBSERVER	ZEISS	Axio Observer 443

RESOURCE AVAILABILITY

Lead contact
Further information and requests for resources and reagents should be directed to and will be fulfilled by the lead contact, Chiara Mozzetta (chiara.mozzetta@uniroma1.it).

Materials availability
Materials generated as part of this study can be requested from the lead contact using standard Material Transfer Agreement (MTA).

Data and code availability
RNA-seq and RIP-seq data have been deposited at NCBI's Gene Expression Omnibus (GEO) repository and are publicly available as of the date of publication. Accession numbers are listed in the key resources table. The paper does not report original code. Any additional information required to reanalyze data reported in this paper is available from the lead contact upon request.

EXPERIMENTAL MODEL AND SUBJECT DETAILS

Cell lines
All cell lines were maintained in a humidified incubator at 37°C with 5% CO2. Primary human skeletal muscle myoblasts (HSMMs) were cultured in growth medium (SkGM-2 Bullet Kit, Lonza). HEK293T cells (kindly gifted by Dr. Slimane Ait-Si-Ali) for the production of lentiviral particles were cultured in Dulbecco's modified Eagle's medium (DMEM) (Sigma-Aldrich, D5671), supplemented with 10% FBS (Corning, 35-015-CV), 2 mM L-glutamine and 100 U/ml penicillin/streptomycin. ARMS cell lines RH30 and RH41 were kindly provided by Rossella Rota (Bambino Gesù Children's Hospital, Rome, Italy). RH30 and RH41 were maintained in RPMI 1640 with L-glutamine (Sigma-Aldrich, R8758) supplemented with with 1% penicillin/streptomycin and 10% FBS (Corning, 35-015-CV). Cells were treated with 2μM UNC0642 and 10 μM A366. RH30 and RH41 were treated with the indicated concentration of RX-5902, dissolved in DMSO (Chemietek, CT-RX5902 Lot 01). Control cells were treated with equivalent volumes of DMSO (Sigma-Aldrich). For RX-5902 treatments we prepared 1000X working stock solutions for all the tested concentrations. Therefore, we added, at maximum, a 0.1% of DMSO in the final volume of culture medium.

Cell lines were not specifically authenticated by STR, but routinely assessed for cell morphology, adherence rate, and cell viability. Also, ARMS cell lines were routinely assessed for the expression of PAX3-FOXO1 and myogenic markers. Expression of myogenic markers has been constantly verified for HSMMs, which were also regularly tested for their ability to differentiate into mature myotubes. Sex of the cells: HEK293T originate from a female fetus; RH30 derive from a bone marrow metastasis of 16-year-old male (Hinson et al., 2013); RH41 derive from a lung metastasis of a 7-year-old female (Hinson et al., 2013). The sex for primary HSMMs is unknown, they derive from adult donors with no precise sex specification at purchase.

Several first passage aliquots of each cell line were stored in liquid nitrogen for subsequent assays.

Immunodeficient mice
All animal procedures were approved by Italian Ministry of Health and Istituto Superiore di Sanità; approval number 7FF2C.7-EXT.9.

Female Balb/c nude mice (6/7 weeks old) were obtained from (Envigo) and maintained under specific pathogen–free conditions in a temperature- and humidity-controlled environment (Allevamenti Plaisant, Castel Romano, Italy).

METHOD DETAILS

Cells transfection
RH30 and RH41 cells were transfected with 100nM of human DDX5 specific siRNA (siDDX5 UTR and siDDX5 CDS, Sigma-Aldrich) or scrambled control siRNA (siCTR) (siRNA universal negative control, Sigma-Aldrich) using Lipofectamine 2000 (Invitrogen) according to the manufacturer's protocol. Transfection with siRNAs was executed when cultured cells reached a confluency of 60% in 6 well plates. Transfection was carried out according to our adapted protocol in RPMI growth medium for 4–6 hours at 37°C. Transfection was then stopped by removing the growth medium and replacing it with RPMI with 10% fetal bovine serum. RNA or protein were isolated 72 h post-transfection for all assays. The targeted sense and antisense strands are shown below:

siDDX5 UTR
Sense: 5′-AACCGCAACCAUUGACGCCAU-3′
Antisense: 5′-AUGGCGUCAAUGGUUGCGGUU-3′
siDDX5 CDS
Sense: 5′-GGCUAGAUGUGGAAGAUGU-3′
Antisense: 5′-ACAUCUUCCACAUCUAGCC-3′

Cell Reports
Report

CellPress
OPEN ACCESS

Short hairpin (sh)RNA lentivirus production and cell infections

Lentiviruses were produced in HEK293T packaging cells seeded in 100 mm culture dishes and transfected in 10mL of DMEM medium, using lipofectamine 2000 (Thermo Fisher Scientific), with lentiviral packaging vectors psPAX2 (7 μg; Addgene) and pMD2.G (3,5 μg; Addgene) and 10 μg lentiviral expression constructs shRNA pLKO.1-puro (EHMT2 Mission shRNA, Sigma-Aldrich, TRCN0000115671, GenBank: NM_025256). For DDX5 knockdown the custom sequence AACCGCAACCAUUGACGCCAU (Sigma-Aldrich DDX5 Mission shRNA plasmid DNA, GeneBank: NM_004396) was cloned in the pLKO.1-puro vector. The non-silencing shCTR (mission control shRNA plasmid DNA) was purchased from Sigma-Aldrich. pLKO.1-neo vector encoding for a Tet-On-shEHMT2 was described in (Tu et al., 2018) and provided by Prof. Linda Penn. Transfection medium was replaced 24 h later with new complete DMEM and 48 h after transfection the lentiviral containing medium was collected, spun to remove cell debris, and the supernatant filtered through a 0.45 μm low protein binding filters. Viral aliquots immediately stored at −80°C. RH30 and RH41 target cells were plated in a 100 mm dish ($1,5 \times 10^6$ cells) and, 24 h later, were infected with lentiviral pLKO.1-puro vectors expressing specific shRNA sequences for 24 h in the presence of polybrene (8μg/ml; Sigma-Aldrich). After further 24 hrs, RH30 and RH41 cells were selected with 1 μg/mL puromycin (Sigma-Aldrich, P8833), or 200ug/L of G418 (Sigma-Aldrich, A1720), for 3 days. Cells were harvested at different time points for subsequent experiments.

In vitro proliferation assays

Cells transfected with siRNA *DDX5* and cells transduced with lentivirus *shRNA EHMT2* were seeded in 6-well plates ($1.8 \ 10^5$ cells per well) and cell proliferation was evaluated by counting trypsinized cultures at 1, 2 and 3 days in RH30 and RH41 cells. In EHMT2 rescue assays, cells were counted at 1 and 2 days post transfection. For RX-5902 experiments, RH30 and RH41 cells proliferation was evaluated by counting trypsinized cultures at 1, 2 and 3 days post-treatment.

Measurement of the stability and half-life of *EHMT2* mRNA

Cells were treated with α-amanitin (25ug/ml) for 0, 4 and 8 hours, upon 72h after siRNA transfection, to determine the stability and half-life of *EHMT2* mRNAs. RNA was isolated as described below and qRT-PCR was used to determine the levels of *EHMT2*. Half-life was calculated using the formula $t \frac{1}{2} = Ln2/K_{decay}$, as described in (Chen et al., 2008).

RNA extraction and quantitative real-time PCR (qRT-PCR)

Cells were harvested and centrifuged at 3000 rpm for 5 min at 4°C. Supernatant was then removed and cell pellet was resuspended in 1 mL of ice-cold PBS and centrifuged at 2000 rpm for 5 min at 4°C. After removing the supernatant, cell pellet was resuspended in 1 mL of TRI Reagent (Sigma aldrich) and RNA extraction was carried out following manufacturer's protocol.

For analysis of spliced vs unspliced EHMT2 RNA levels, *Quick*-RNA Miniprep Kit (Zymo-Research) was used and RNA was treated with DNAse I, following manufacturer's protocol.

Quantity of RNA samples were assessed with Nano-Drop analysis (NanoDrop Technologies). cDNA synthesis was performed using a High-Capacity cDNA Reverse Transcription Kits (Applied Biosystems). qRT-PCR was performed with a Step-One plus Real-Time PCR System (Applied Biosystems) to analyze relative gene expression levels using SYBR Green Master mix (Applied Biosystems) following manufacturer indications.

PCR amplification was performed as follows: 95°C 5 minutes, followed by 95°C for 10s, annealing at 60°C for 10s, followed by 45 cycles at 72°C for 10s. Melting curves were generated and tested for a single product after amplification. Expression of each target was calculated using the $2^{-\Delta\Delta Ct}$ method and expressed as a relative mRNA expression. Relative expression values were normalized to the housekeeping gene GAPDH. qRT-PCR was done using reaction duplicates and three independent biological replicates were done for each analysis. Error bars indicate the mean ± standard deviation.

The primers we used are reported in Table S2.

Protein extraction and Western blotting

Cells were harvested and centrifuged at 3000 rpm for 5 min at 4°C. Supernatant was then removed and cell pellet was resuspended in 1 mL of ice-cold PBS and centrifuged at 2000 rpm for 5 min at 4°C. After removing the supernatant, cell pellet was resuspended in RIPA lysis buffer supplemented with protease inhibitor cocktail and phosphatase inhibitors (Roche) and incubated in ice for 30 min. Samples were then sonicated in a water bath for 10 min (30 sec ON/30 sec OFF) and centrifuged at 15000 rpm for 15 min at 4°C. Supernatant was then transferred in a new tube and proteins were quantified by BCA assay (Thermo Fisher Scientific) according to the manufacturer's protocol.

For cytosolic and nuclear extraction, cell pellet was resuspended in nuclear fractionation buffer (20mM Hepes pH 8, 10mM KCl, 2mM MgCl$_2$, 1mM EDTA, 1mM EGTA, 1mM DTT and protease inhibitors) and incubated on ice for 15 minutes. Cell suspension was then passed 10 times through a 1mL syringe with 26-gauge needle and then left on ice for additional 20 minutes before centrifugation at 750g for 5 minutes. The supernatant is the cytosolic extract (CE). The nuclear pellet was then washed 2 times with the nuclear fractionation buffer and, after centrifugation at 750g for 10 minutes, was resuspended with TBS containing 0.1% SDS and sonicated to obtain the nuclear extract (NE).

Cell lysates were resolved on 4%–20% Mini-PROTEAN TGX gels (Bio-Rad Laboratories) and then transferred to nitrocellulose membrane (Amersham) using Trans-Blot Turbo Transfer system (Bio-Rad Laboratories). Membranes were blocked with 5% nonfat

dried milk in Tris-buffered saline/Tween (TBS-T; 0.1%) for 1 hour at room temperature with gentle shaking, followed by overnight incubation at 4°C with various antibodies. The primary antibodies we used were: DDX5 (Cell Signalling, #9877), EHMT2 (Cell signalling, #3306), FOXO1 (Cell Signalling, #2880), p-AKT (Ser473) (Cell signaling, #4058), AKT (Cell signaling #4685), PARP (Cell signaling #9542), cleaved caspase 7 (Cell signaling #8438), cleaved caspase 9 (Cell signaling #9505), MYOD (Santa Cruz Biotechnology, C-20), myogenin (DSHB, F5D), GAPDH (Sigma, G9545), α-tubulin (Sigma-Aldrich, T5168). Membranes were then incubated with HRP-conjugated secondary antibodies (IgG-HRP, Sigma-Aldrich) for 1 hour at RT and after incubation the blots were developed in an ECL detection solution (Clarity Max ECL substrate, Bio-Rad Laboratories) and signal was detected using ChemiDoc (BioRad Laboratories).

Mouse xenograft experiments

2×10^6 shCTR and shDDX5 RH30 cells were injected subcutaneously into the flank of mice and, once tumors were palpable, they were measured every other day by measuring 2 diameters (d1 and d2) in right angles using a digital caliber. Total tumor volume was then calculated by the formula $V = (4/3)\pi r^3$; $r = (d1 + d2)/4$. On day 21 after the injections, mice were euthanized, and resected tumors were fixed in formalin or immersed in liquid nitrogen and stored at -80 degrees. For western blot analysis, tumors were disrupted with a mortar and pestle, followed by sonication in RIPA buffer supplemented with proteinase and phosphatase inhibitors (Roche). Formalin-fixed tumor tissues were embedded in paraffin and sections were stained with hematoxylin and eosin using standard techniques (data not shown). Tissue sections were deparaffinized, rehydrated, and heated at 95°C for 20 min in pH 6 antigen retrieval buffer. Slides were blocked and incubated with Ki67 antibody (Abcam 15580) overnight at 4°C, then incubated with the secondary antibody (Alexa Fluor 488, Thermo Fisher Scientific). Nuclei were counterstained with DAPI (Sigma). Images were acquired using Axio Observer 443 microscope (ZEISS) and analyzed by ZEN 3.0 (Blue edition) software.

Co-immunoprecipitation

Co-immunoprecipitation was carried out through magnetic separation. RH30 and RH41 cells were centrifuged at 1200 rpm for 5 min at 4°C, resuspended in lysis buffer (10 mM Tris pH 8, 10 mM NaCl, 0.1 mM EDTA pH 8, 0.1 mM EGTA) with protease inhibitor (Roche) and then incubated on ice for 30 min. A dounce homogenizer was used to mechanically help cell lysis. 10% NP-40 was added to a final concentration of 0,5% and then samples were vortexed and incubated on ice 2–3 min. Samples were then centrifuged at 800g for 5 min at 4°C in order to pellet nuclei. Nuclei were resuspended in nuclei lysis buffer (20 mM Tris pH 8, 400 mM NaCl, 1 mM EDTA pH 8, 1 mM EGTA) with protease inhibitor (Roche) and incubated for 10 min on ice to increase lysis efficiency. Lysates were then sonicated for 10 min (30 sec On/30 sec OFF at high intensity) and then centrifuged at top speed for 20 min at 4°C. Supernatant, containing nuclear extract (NE), was then transferred into a new tube: 50 µL on NE was saved to use as input and to quantify NE concentration. NE was then precleared with 10 µL protein A/G magnetic beads (Thermo Fisher Scientific), washed with IP lysis buffer (50 mM Tris pH 8, 150 mM NaCl, 1 mM EDTA pH 8, 1 mM EGTA) for 2 hrs at 4°C on rotating wheel. After preclearing, NE was diluted 1:5 in IP buffer with protease inhibitor (Roche) and incubated overnight at 4°C on rotating wheel with 10 ug of EHMT2 antibody (Abcam, ab185050) or FOXO1 (Cell Signalling, #2880). The following day pre-blocked protein A/G magnetic beads (Thermo Fisher Scientific) were added to each sample and incubated for 2 hrs at 4°C on rotating wheel. Samples were then washed six times, one wash every 5 min, with IP buffer. At the end, beads were separated on a magnet and the immunocomplexes were resuspended with IP buffer and LSB buffer (Biorad Laboratories) for further analysis.

For RNase treatment of co-immunoprecipitated samples, immunoprecipitated complexes were washed three times with IP buffer. These complexes were then equally divided and resuspended into 1mL of IP buffer with or without 150ug/ml of RNase A. After incubation in RNase A for 30min at 37°C, the immunoprecipitated complexes were washed three times with IP buffer. After the last wash the samples were eluted as described above.

Cross-linking immunoprecipitation (CLIP) assay

CLIP experiments were performed on nuclear extract obtained with some modification of the Rinn et al. protocol (Rinn et al., 2007). Briefly, RH30 cells were washed with PBS and crosslinked with UV rays and collected in Buffer A (20mM Tris HCl pH8.0, 10mM NaCl, 3mM MgCl2, 0.1% NP40, 10% Glycerol, 0.2mM EDTA, 0.4mM PMSF, 1XPIC). Cells were centrifuged at 500 xg for 10 minutes and resuspended in Buffer A, the nuclei pellet was resuspended in NP40 lysis buffer (50mM HEPES-KOH, 150Mm KCL, 2Mm EDTA, 1Mm NaF, 0,5% NP40 PH 7.4, 0,5Mm DTT, 100X PIC). Break with 7mL Dounce (tight pestel/B pestel) and centrifuged at max speed for 20 minutes at 4°C. The supernatant was quantified with BCA assay. 10% of the nuclear extract was collected for Input. Protein A/G Magnetic beads (Thermos Scientific) were washed with PBS tween 0,02% (1X PBS, 0,02% Tween-20) were incubate in PBS Tween 0,02% with 10ug IgG and DDX5 (Abcam, ab10261) antibody on rotating wheel 1 h at RT. The NE was divided in each sample with the coated beads (beads+ Ab) and incubate on rotating wheel ON at 4°C. The beads were washed 3 times with the NP40 High Salt Buffer 0.5X (25 mM HEPES-KOH pH7.5, 250 mM KCL, 0.025% NP40), 2 times with PNK Buffer (50mM Tris-HCL, 50Mm NaCl, 10mM MgCl2 pH7.5) and resuspended with NP40 lysis buffer. ¼ was taken for protein analysis where was add LSD 5X and DTT 100X, for 5 minutes at 95°C. The rest was used for RNA analysis: the beads were resuspended in proteinase K buffer (200MM Tris-HCL, 300 mM NaCl, 25 mM EDTA, 2%SDS pH 7.5).

Cell Reports
Report

CellPress
OPEN ACCESS

RNA immunoprecipitation

For RIP from nuclear extracts, RH30 cells were resuspended in buffer A/NT1 (20mM Tris HCl pH8.0, 10mM NaCl, 3mM MgCl2, 0.1% NP40, 10% Glycerol, 0.2mM EDTA, 0.4mM PMSF, 1XPIC) kept on ice for 15 minutes and then centrifuged at 2000 rpm for 5 minutes at 4°C to pellet the nuclei. The supernatant was collected as cytoplasmic extract. The pellet was rewashed with buffer A for 3 times. The pellet was resuspended in NT2/Wash buffer (50mM Tris pH7.4, 150mM NaCl, 1mM MgCl2, 0,5% NP40, 20mM EDTA, 1X PIC, 1X PMSF, 1 mM DTT), broken with 7mL dounce and centrifuged at 14000 rpm for 30 minutes at 4°C. Protein A/G Magnetic beads (Thermo Fisher Scientific) were incubated with 10ug of IgG and DDX5 (Abcam, ab10261) antibody on rotating wheel O/N at 4°C while the nuclear extract (NE) was precleared with the beads. 10% of the NE was collected for INPUT. The NE was incubated on rotating wheel ON at 4°C. The beads were washed with NT2 buffer. RIP qPCR results were represented as percentage of IP/input signal (% input) *vs* IgG.

RIP sequencing

Nuclear RNA was extracted and quantified as previously described. RIP-Seq libraries preparation and sequencing was performed by the IGA Technology Services (Udine, Italy) using the Trio RNA-Seq kit (Tecan Genomics, Redwood City, CA) according to manufacturer's instructions. The final libraries for unstranded single-end sequencing of 75 base pairs were carried out on an Illumina NextSeq 500 (Illumina, San Diego, CA) with an average of 32.5 million of reads per sample. Processing raw data for both format conversion, demultiplexing and evaluation of reads quality were performed as described for RNA-seq in siDDX5 FP-RMS.

Preprocessed reads were mapped to the human Ensembl GRCh38 build reference genome using *STAR* version 2.6.1d (Dobin et al., 2013) using Gene annotations corresponding to the Ensembl annotation release 96 which was used to build a transcriptome index and provided to *STAR* during the alignment.

Each resulting BAM file were sorted using *samtools* 1.10 (Li et al., 2009) and then converted in scaled bigWig coverage tracks for visualization in the Integrative Genomics Viewer software.

DDX5 enriched regions were identified using MACS version 2.2.7.1 (Zhang et al., 2008) with Q-value cutoff of 0.05 by comparing the RIP-seq data to its matching input control.

The resulting filtered peak sets were assigned to a genomic region and associated with genes and genomic features using *R* environment with Bioconductor (Gentleman et al., 2004) packages *GenomicRanges* and *GenomicFeatures* (Lawrence et al., 2013). Genes were clustered by functional annotation using Bioconductor *R* package *clusterProfiler* version 3.14 (Yu et al., 2012) with annotation of Gene Ontology Database (Ashburner et al., 2000).

RNA-sequencing
RNAseq in siDDX5 FP-RMS

Total RNA was extracted and quantified as previously described. RNA-Seq libraries preparation and sequencing was performed by the IGA Technology Services (Udine, Italy) using the Illumina TruSeq Stranded mRNA Kit (Illumina, San Diego, CA) according to manufacturer's instructions. The final libraries for paired-end sequencing of 150 base pairs were carried out on an Illumina NovaSeq6000 (Illumina, San Diego, CA) with an average of 55 million of reads per sample. Processing raw data for both format conversion and demultiplexing were performed by *Bcl2Fastq* version 2.20 of the Illumina pipeline. Reads quality was evaluated using *FastQC* (version 0.11.8, Babraham Institute Cambridge, UK) tool, then adapter sequences were masked with *Cutadapt* version 1.11 (Martin, 2011) from raw fastq data using the following parameters: *–anywhere* (on both adapter sequences) *–overlap 5 –times 2 –minimum-length 35 –mask-adapter*.

Reads were mapped to the human Ensembl GRCh38 transcriptome index (release 96) using *kallisto* (version 0.46.0) (Bray et al., 2016). The following flags were used for *kallisto*: *-b 30 –bias*. Gene-level normalization and differential gene expression analysis were performed using Bioconductor (Gentleman et al., 2004) R (version 3.6.2) package *DESeq2* version 1.26 (Love et al., 2014) accounting for the presence of batch effects. The figures were obtained using the *R* environment with package *ggplot2* version 3.3.0 and *pheatmap* version 1.0.12.

RNAseq in shEHMT2 FP-RMS

RNA-seq libraries from total RNA (100 ng) from each sample were prepared using QuantSeq 3′mRNA-Seq Library prep kit (Lexogen, Vienna, Austria) according to manufacturer's instructions, at Telethon Institute of Genetics and Medicine (TIGEM, Naples, Italy). The amplified fragmented cDNA of 300 bp in size were sequenced in single-end mode using the NextSeq500 (Illumina) with a read length of 75 bp. Reads quality was evaluated using *FastQC* (version 0.11.8, Babraham Institute Cambridge, UK) tool and was trimmed using *TrimGalore* software to remove adapter and low-quality bases (Q < 20). Then reads were mapped to the human Ensembl GRCh38 build reference genome using *STAR* version 2.5.0a (Dobin et al., 2013) using Gene annotations corresponding to the Ensembl annotation release 96 which was used to build a transcriptome index and provided to *STAR* during the alignment.

The same gene annotations were used to quantify the gene-level read counts using *HTSeq-count* version 0.8.0 (Anders et al., 2015) script, subsequently the data normalization and differential analysis for gene expression were performed using Bioconductor (Gentleman et al., 2004) R package *edgeR* version 3.28 (Robinson et al., 2010).

Gene set enrichment analysis

In order to understand biological meaning of the differentially expressed genes the resulting filtered (Benjamini-Hochberg false discovery rate (FDR) adjusted for multiple hypothesis testing p-value < 0.05) genes were clustered by functional annotation using

CellPress
OPEN ACCESS

Cell Reports
Report

Bioconductor *R* package *clusterProfiler* version 3.14 (Yu et al., 2012) with annotation of Gene Ontology Database (Ashburner et al., 2000) and with annotation of Kyoto Encyclopedia of Genes and Genomes (KEGG) (Ogata et al., 1999) for pathways. Gene Set Enrichment Analysis (GSEA) (Subramanian et al., 2005) with pre-ranked, "classic" mode with 10,000 permutations was used to assess the enrichment of the gene profile of siDDX5 or shEHMT2 samples compared to control samples in the curated "hallmark" and "C2" gene set collections (BROAD molecular signature database, MSigDb version 6.2).

QUANTIFICATION AND STATISTICAL ANALYSIS

Data were analyzed using Prism (version 6.0; GraphPad Software Inc.), and images were compiled in Adobe Illustrator (CC 2017; Adobe Systems). Results are presented as mean $\pm$ SEM from at least 3 independent experiments. Statistical analysis was conducted using paired or unpaired Student's t-test, one-way ANOVA or 2-way ANOVA, as indicated in the figure legends. *p* value of less than 0.05 was considered statistically significant. *$p < 0.05$; **$p < 0.01$; ***$p < 0.001$; ****$p < 0.0001$ and the exact values are indicated on the corresponding graphs.